Spatiotemporal analysis of axonal autophagosome–lysosome dynamics reveals limited fusion events and slow maturation

Sydney E. Cason[a,†], Saurabh S. Mogre[b,†], Erika L. F. Holzbaur[a], and Elena F. Koslover[b,*]
[a]Department of Physiology, University of Pennsylvania, Philadelphia, PA 19104; [b]Department of Physics, University of California, San Diego, La Jolla, CA 92093

ABSTRACT **Macroautophagy is a homeostatic process required to clear cellular waste. Neuronal autophagosomes form constitutively in the distal tip of the axon and are actively transported toward the soma, with cargo degradation initiated en route. Cargo turnover requires autophagosomes to fuse with lysosomes to acquire degradative enzymes; however, directly imaging these fusion events in the axon is impractical. Here we use a quantitative model, parameterized and validated using data from primary hippocampal neurons, to explore the autophagosome maturation process. We demonstrate that retrograde autophagosome motility is independent of fusion and that most autophagosomes fuse with only a few lysosomes during axonal transport. Our results indicate that breakdown of the inner autophagosomal membrane is much slower in neurons than in nonneuronal cell types, highlighting the importance of this late maturation step. Together, rigorous quantitative measurements and mathematical modeling elucidate the dynamics of autophagosome–lysosome interaction and autophagosomal maturation in the axon.**

Monitoring Editor
Leah Edelstein-Keshet
University of British Columbia

Received: Mar 29, 2022
Revised: Jul 21, 2022
Accepted: Aug 23, 2022

INTRODUCTION

Neurons are terminally differentiated cells that last throughout the lifetime of the organism. One important pathway for maintaining cellular health and homeostasis over this long time period is macroautophagy (hereafter: autophagy), the formation of "self-eating" double-membraned organelles that engulf and degrade cellular waste in order to recycle macromolecular components (Figure 1a) (Yin *et al.*, 2016). Defects in neuronal autophagy are implicated in most neurodegenerative disorders, including Parkinson's disease, Alzheimer's disease, and amyotrophic lateral sclerosis (Wong and Holzbaur, 2015). Further, genetically blocking autophagic vacuole (AV) formation causes neurodegeneration in mice (Hara *et al.*, 2006; Komatsu *et al.*, 2006). Given the importance of autophagy in the maintenance of neuronal homeostasis, it is essential to gain a quantitative understanding of the pathway.

Neuronal AVs form constitutively at presynaptic sites including the distal tip of the axon (Figure 1b), where they clear aged proteins and organelles (Maday *et al.*, 2012; Goldsmith *et al.*, 2022). However, the vast majority of protein and organelle production occurs in the soma (Misgeld and Schwarz, 2017; Farfel-Becker *et al.*, 2019; Koltun *et al.*, 2020). Thus, neuronal AVs must traverse the length of the axon, up to 1 m in humans, to recycle their cargo (Maday and Holzbaur, 2014; Stavoe and Holzbaur, 2019). AVs acquire molecular motors after formation to drive their transit to the soma (Fu *et al.*, 2014; Cheng *et al.*, 2015; Cason *et al.*, 2021). En route, axonal AVs mature by fusing with endolysosomes, organelles containing the digestive enzymes necessary to break down autophagosomal cargo (Maday *et al.*, 2012; Cason *et al.*, 2021). Degradatively active

This article was published online ahead of print in MBoC in Press (http://www.molbiolcell.org/cgi/doi/10.1091/mbc.E22-03-0111) on August 31, 2022.

Conflict of interest: The authors declare no competing financial interests.

†These authors contributed equally.

Author contributions: S.E.C.: resources, data curation, formal analysis, validation, investigation, visualization, methodology, project administration, writing—original draft and review/editing; S.S.M.: conceptualization, resources, formal analysis, investigation, software, validation, visualization, methodology, project administration, writing—original draft and review/editing; E.L.F.H.: supervision, funding acquisition, project administration, writing—original draft and review/editing; E.F.K.: conceptualization, supervision, software, funding acquisition, project administration, writing—original draft and review/editing.

*Address correspondence to: Elena F. Koslover (ekoslover@ucsd.edu).

Abbreviations used: AEP, asparagine endopeptidase; AV, autophagic vacuole; CTSL, cathepsin L; DRG, dorsal root ganglia; IAM, inner autophagosomal membrane; LAMP1, lysosome-associated membrane protein 1; SD, standard deviation; SEM, standard error of the mean.

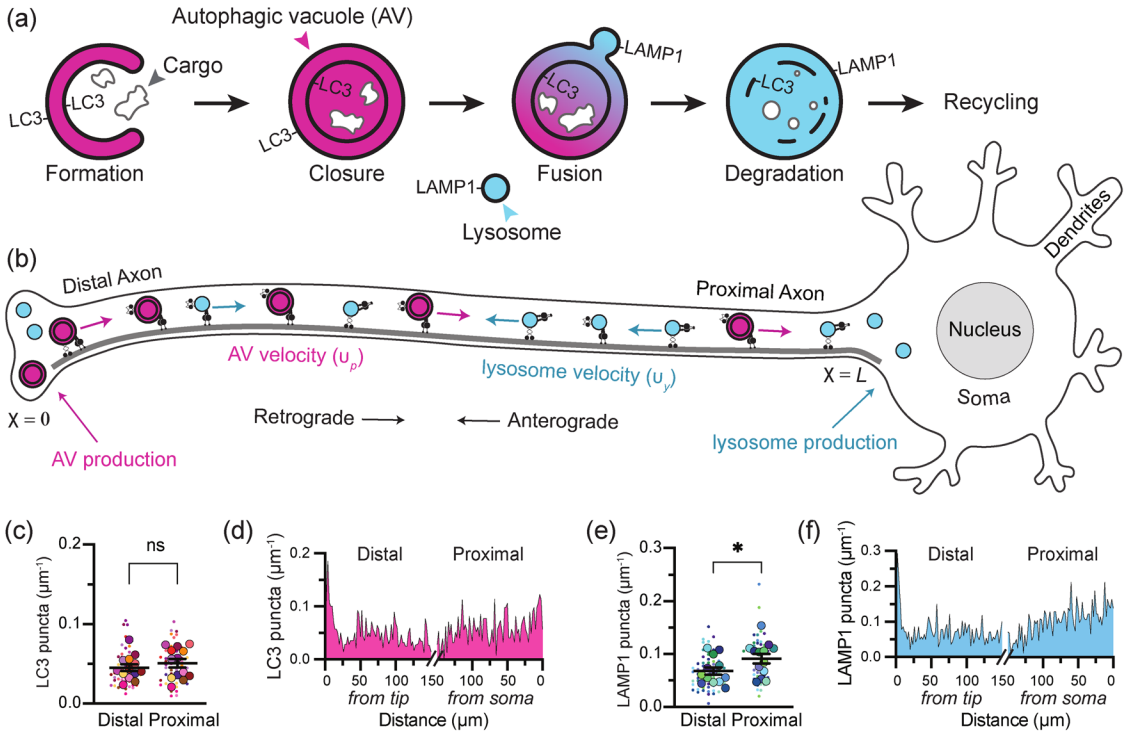

FIGURE 1: Neuronal autophagosomes form in the distal axon and fuse with lysosomes during transit to the soma. (a) Schematic illustrating the autophagy pathway. The developing phagophore engulfs cargo and seals its double membrane to form an AV. The inner and outer membranes are initially decorated with lipidated LC3; however, the LC3 on the outer membrane is cleaved off following closure. AVs fuse with late endosomes and LAMP1-containing lysosomes to acquire degradative enzymes. The autophagic cargo is then broken down and the resulting macromolecules are recycled by the cell. (b) Schematic illustrating axonal autophagy. AV biogenesis primarily occurs in the distal tip of the axon, while lysosome biogenesis occurs in the soma. AVs are transported retrograde toward the soma, while lysosomes move processively in both anterograde and retrograde directions. During this microtubule-based transport, the two organelles encounter one another and have some probability of fusing to facilitate AV maturation. In this study, the distal axon is defined as within 250 μm of the axon tip and the proximal axon as within 250 μm of the soma, with the total axon length ($x = L$) determined experimentally. (c) Linear density of endogenous LC3 puncta, detected with RRID:AB 881433 or RRID:AB 11150489. $n = 13$ trials; unpaired t test ($p = 0.4504$). (d) Spatially resolved density of LC3+ puncta, normalized to bin size and cell number. $n = 999$ puncta in 131 cells; 2 μm bins. (e) Linear density of LAMP1 puncta, detected with RRID:AB 1026176 or RRID:AB 2134500. $n = 13$ trials; unpaired t test ($p = 0.0489$). (f) Spatially resolved density of LAMP1 puncta, normalized to bin size and cell number. $n = 1627$ puncta in 131 cells; 2 μm bins. Small dots throughout represent data from individual cells, while the larger outlined dot of the same color represents the mean from that trial. Statistics were performed using the means from the trials. Bars show mean ± SEM.

endolysosomes, known as lysosomes, are produced in the soma and actively delivered to the axon to fuse with AVs (Farfel-Becker *et al.*, 2019; Roney *et al.*, 2021). The maturation of AVs during transport from the axonal tip to the soma is a well-studied phenomenon. However, it has proven experimentally difficult to study the fusion between AVs and endolysosomes along the axon, precluding a quantitative understanding of the spatiotemporal dynamics of maturation.

Mathematical modeling of organelle transport and interactions allows for a quantitative connection from single organelle parameters (such as stopping rates and fusion probabilities) to the cellular-scale distribution of components (Williams *et al.*, 2016; Mogre *et al.*, 2020, 2021; Agrawal and Koslover, 2021). We sought to dissect the mechanisms underlying autophagosomal maturation in the axon by developing a spatially resolved quantitative model of this phenomenon, parameterized from experimental data.

We construct a comprehensive model of organelle transport, interaction, and maturation during axonal autophagy. The model reproduces features of organelle distribution and maturation observed using endogenous staining and live-cell imaging in primary hippocampal neurons. We incorporate the branched geometry of neuronal axons and highlight the role of parameters including production rates, fusion probability, and motility dynamics. AV–endolysosome fusion is followed by degradation of the inner AV membrane before cargo breakdown can begin; our imaging and quantitative model highlight the latter step of maturation as rate-limiting in neurons. The two-way interplay between experimental measurements and mathematical modeling presented in this work sheds light on the multistep mechanisms and spatiotemporal distribution of neuronal autophagosome maturation.

RESULTS

AVs mature in the axon under endogenous conditions

Previous studies in vitro and in vivo have detected AV maturation by assessing colocalization between fluorescent markers for lysosomes and AVs (Maday *et al.*, 2012; Stavoe *et al.*, 2016; Hill *et al.*, 2019; Cason *et al.*, 2021). Typically, an Atg8 orthologue (e.g., LC3) is used to label AVs. Lysosomes are commonly labeled by lysosome-associated membrane protein 1 (LAMP1); however, LAMP1 also localizes to late endosomes and Golgi-derived vesicles, especially when

overexpressed (Cheng *et al.*, 2018; Farfel-Becker *et al.*, 2019; Lie *et al.*, 2021). Additionally, we worried that exogenous overexpression of LC3 or LAMP1 may affect the quantity of AVs and/or endolysosomes, given their roles in organelle biogenesis and turnover (Yu *et al.*, 2010; Ma *et al.*, 2012; Shibutani and Yoshimori, 2014; Stavoe *et al.*, 2019). We therefore performed rigorous immunofluorescence measurements to determine the density and spatial distribution of LC3-containing (LC3+) and LAMP1-containing (LAMP1+) organelles in the axon under endogenous conditions.

In brief, we plated primary embryonic rat hippocampal neurons on glass coverslips, fixed and permeabilized without detergents after 7–10 days in vitro, and probed with validated antibodies to endogenous autophagosomal and lysosomal proteins (Supplemental Figure S1). The linear densities of LC3 puncta in the distal and proximal axon were roughly the same, with an average of one punctum every 20 µm (≈0.05 μm^{-1}) (Figure 1c), consistent with what we detect using fluorescently tagged LC3 in live neurons (Supplemental Figure S1). LAMP1 puncta were more dense (Figure 1e) and marginally higher in the proximal axon (one punctum every ≈10 µm; ≈0.09 μm^{-1}) than in the distal axon (one punctum every ≈15 µm; ≈0.07 μm^{-1}). Both LC3 and LAMP1 accumulated mildly in the axon tip (Figure 1, d and f). These density measurements are consistent with published live-cell measurements in a variety of neuronal cell types (Lee *et al.*, 2011; Maday *et al.*, 2012; Farfel-Becker *et al.*, 2019; Boecker *et al.*, 2020).

LAMP1-labeled compartments are degradatively competent. Some recent studies have proposed that only a small fraction of axonal lysosomes are degradatively competent (Gowrishankar *et al.*, 2015; Cheng *et al.*, 2018; Farfel-Becker *et al.*, 2019). Studies in nonneuronal cells have also proposed a lysosomal activity gradient wherein lysosomes closer to the nucleus are more mature and proteolytically active than those farther from the nucleus (Johnson *et al.*, 2016; Ferguson, 2018). We therefore examined the degradative capacity of lysosomes along the axon by measuring the colocalization between endogenous LAMP1 and the endogenous lysosomal enzymes asparagine endopeptidase (AEP) and cathepsin L (CTSL) (Figure 2, a and d). Across the axon, roughly three-quarters of the LAMP1 colocalized with lysosomal enzymes. Lysosomal proteases require low pH to function, so we probed for the presence of the lysosomal vATPase, which pumps protons across the membrane to achieve and maintain the lysosome's characteristic low pH (≈4.8) (Johnson *et al.*, 2016). The vATPase subunit V1 is cytoplasmic and forms an activated vATPase when interacting with the transmembrane V0 subunit. Therefore colocalization between the V1 subunit (ATP6V1F) and membrane-bound LAMP1 suggests the formation of an active vATPase on the AV membrane. Again, we saw about 80% colocalization in both the proximal and distal axon (Figure 2, e and f). These data suggest that the population of LAMP1-positive (LAMP1+) lysosomes along the axon is primarily mature and degradatively competent.

Most AVs mature along the axon. Next, we quantified colocalization between LC3 and LAMP1 and found that roughly 50% of the AVs in the distal axon colocalized with LAMP1 (Figure 3, a and b). Considering our optical resolution (200 nm), these colocalized puncta likely represent fused or fusing organelles. More AVs were positive for LAMP1 in the proximal axon, implying that an additional ≈25% of AVs fused with a LAMP1+ organelle in the axon shaft during transit to the soma (Figure 3, a and b). About 30% of the LAMP1 in both distal and proximal regions colocalized with LC3, indicating an excess of unfused lysosomes present throughout the axon (Figure 2, g and h).

We also assessed colocalization with lysosomal enzymes and the vATPase. Roughly half of the LC3 puncta in the distal axon colocalized with AEP, CTSL, and ATP6V1F, and colocalization increased in the proximal axon, indicating further fusion of AVs with endolysosomes during translocation toward the soma (Figure 3, c–h). We therefore conclude that half of the axonal AV population fuses with a degradatively active lysosome before leaving the distal axon, while an additional quarter of the population fuses with an active lysosome along the mid-axon before reaching the proximal axon and soma.

Mathematical modeling elucidates interplay of transport and fusion in autophagosome–lysosome distributions

We next proceeded to develop a coarse-grained mathematical model for axonal AV maturation through fusion with endolysosomes. The model is parameterized against experimental data and aims to elucidate how organelle transport and interaction parameters dictate the spatial distribution of lysosomes, AVs, and fusion events.

We first simplify the axonal geometry to a one-dimensional domain of length L = 1055 µm, representing the average length of primary hippocampal axons at 7–10 days in vitro (Supplemental Figure S2a). The model includes the biogenesis of AVs in the distal axon tip (Maday and Holzbaur, 2014) and the production of lysosomes in the soma (Farfel-Becker *et al.*, 2019), along with switches between different motility states (Fu *et al.*, 2014; Cason *et al.*, 2021) and AV–lysosome fusion events (Figure 4). We explore organelle distributions both with stochastic agent-based simulations of discrete particles and in a mean-field sense, by solving for the continuous spatial densities of different organelle states. Given the long lifetime of neuronal cells, we assume that overall spatial distributions of organelles have plenty of time to become established and that we can neglect initial transient behaviors during cell growth. The models thus focus on the steady-state solutions and are independent of initial conditions.

Model for AV transport and distribution. In the model, AVs are formed at the distal axon tip ($x = 0$) at rate k_p^b. Nascent AVs engage in short bidirectional movements or remain relatively stationary (Fu *et al.*, 2014; Cason *et al.*, 2021). This is likely due to short-range, microtubule-based transport, wherein kinesin and dynein motors bound to the organelle may be competing in a "tug-of-war" (Hancock, 2014; Canty and Yildiz, 2020). Using live-cell particle-tracking data, we classify LC3+ AVs in the distal, mid-axonal, and proximal regions as being stationary, bidirectional, or processively motile (Figure 5, a–d; Supplemental Figure S4). Most AVs in the distal axon are stationary or bidirectional, with roughly symmetric bidirectional displacement (Figure 5b). This is in contrast to AVs in the mid- or proximal axon, which are primarily retrograde, meaning that they are moved processively by the cytoplasmic dynein I motor (Canty and Yildiz, 2020; Cason *et al.*, 2021). In the mathematical model, we assume that all motile AVs have a speed of v_p = 0.75 µm/s (Boecker *et al.*, 2020) and neglect the small percentage of processively anterograde AVs.

The spatial densities of retrograde, anterograde, and stationary AVs in the bidirectional state are described by $B_r(x)$, $B_a(x)$, and $B_s(x)$, with rates of switching k_w^b and k_f^b between the different bidirectional states defined in Figure 4. Parameter estimates are listed in Table 1 and detailed in *Materials and Methods*.

Past models of intermittent bidirectional transport (Newby and Bressloff, 2009, 2010; Newby and Keener, 2011; Mogre and Koslover, 2018) show that in the limit where reversal rates are fast

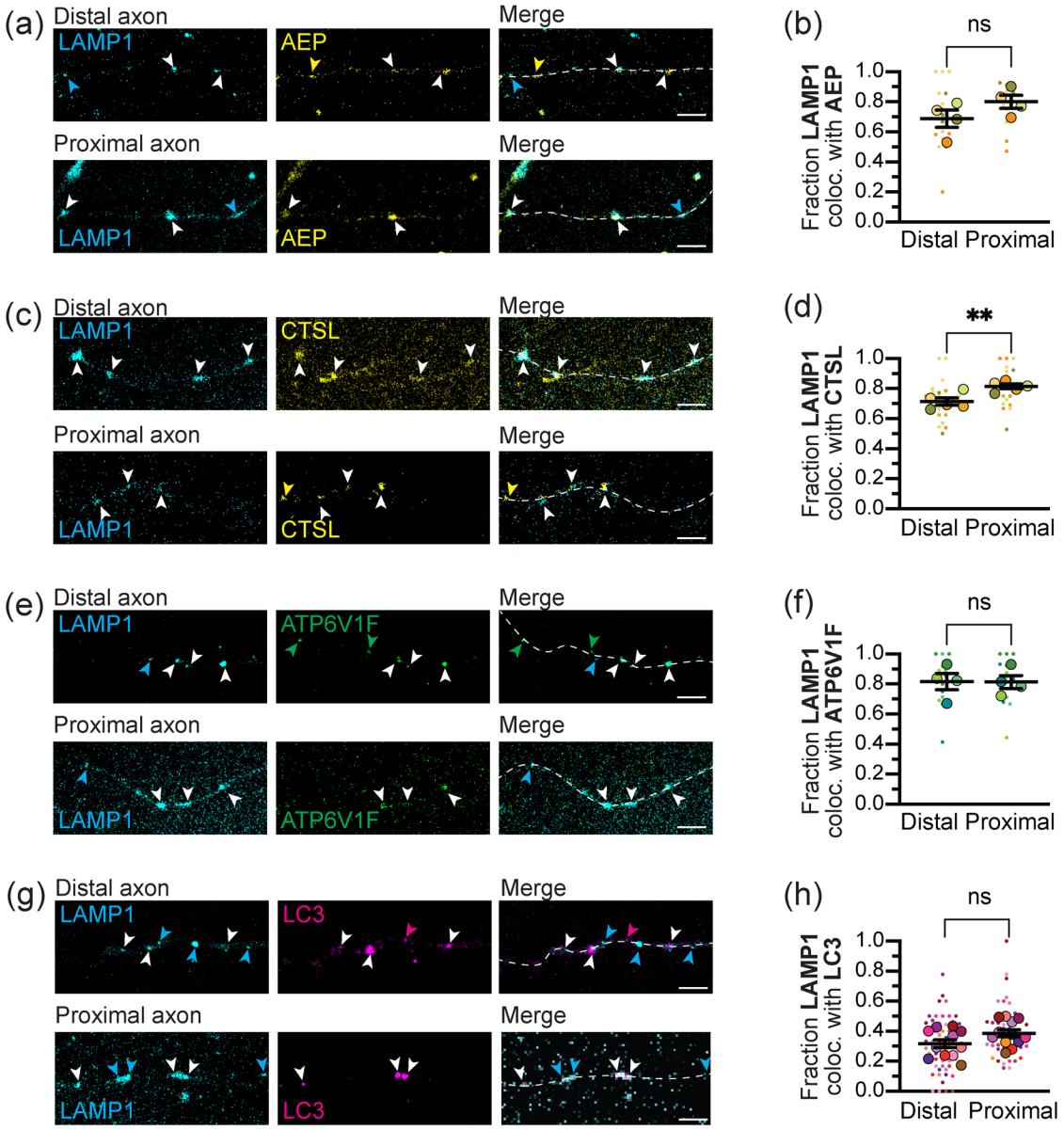

FIGURE 2: Lysosomes throughout the axon are degradatively competent. Maximum projections (a) and quantification (b) showing LAMP1 and asparagine endopeptidase (AEP) overlap in the distal and proximal axon. $n = 4$ trials; unpaired t test ($p = 0.1684$). Maximum projections (c) and quantification (d) showing LAMP1 and cathepsin L (CTSL) overlap in the distal and proximal axon. $n = 5$ trials; unpaired t test ($p = 0.0073$). Maximum projections (e) and quantification (f) showing LAMP1 and V-type proton ATPase subunit F (ATP6V1F) overlap in the distal and proximal axon. $n = 4$ trials; unpaired t test ($p = 0.9588$). Maximum projections (g) and quantification (h) showing LAMP1 and LC3 overlap in the distal and proximal axon. $n = 12$ trials; unpaired t test ($p = 0.8411$). Dashed line represents axon. Cyan arrows, LAMP1 alone; yellow/green/pink arrows, respective marker alone; white arrows, colocalization. Scale bar, 5 μm. Fractions are all over the total LAMP1+ puncta in that region. Small dots throughout represent individual cells, while the larger outlined dot of the same color represents the mean from that trial. Statistics were performed using the means from the trials. Bars show mean ± SEM. Dashed line represents axon. ns, $p > 0.05$; **, $p < 0.01$.

compared with the timescale of encountering targets in the domain, such transport dynamics can be approximated as an effective diffusion and drift in a quasi–steady-state limit. However, the rate of interaction between moving organelles as well as the rate of encounter with stationary structures (such as the distal tip) depend on the detailed motility states of the particles. Here, we choose to include all three bidirectional states (anterograde, retrograde, and stationary) explicitly to enable a direct connection with the observed motility patterns of AVs (Figure 5, a–e).

The modeled bidirectional AVs have a constant rate k_s of switching to a processive retrograde motile state (density $R(x)$) with constant velocity v_p. While only 12.4% of LC3+ puncta are retrograde in the distal axon (Figure 5a), this fraction rises to ≈60% in the mid-axonal and proximal regions (Figure 5, c and d). Past studies of axonal autophagosome dynamics suggested that fusion with an endolysosome was a prerequisite for switching to retrograde motility (Cheng *et al.*, 2015). We analyzed the motility of AVs that did (LysoTracker+) or did not (LysoTracker–) colocalize with LysoTracker, a dye that

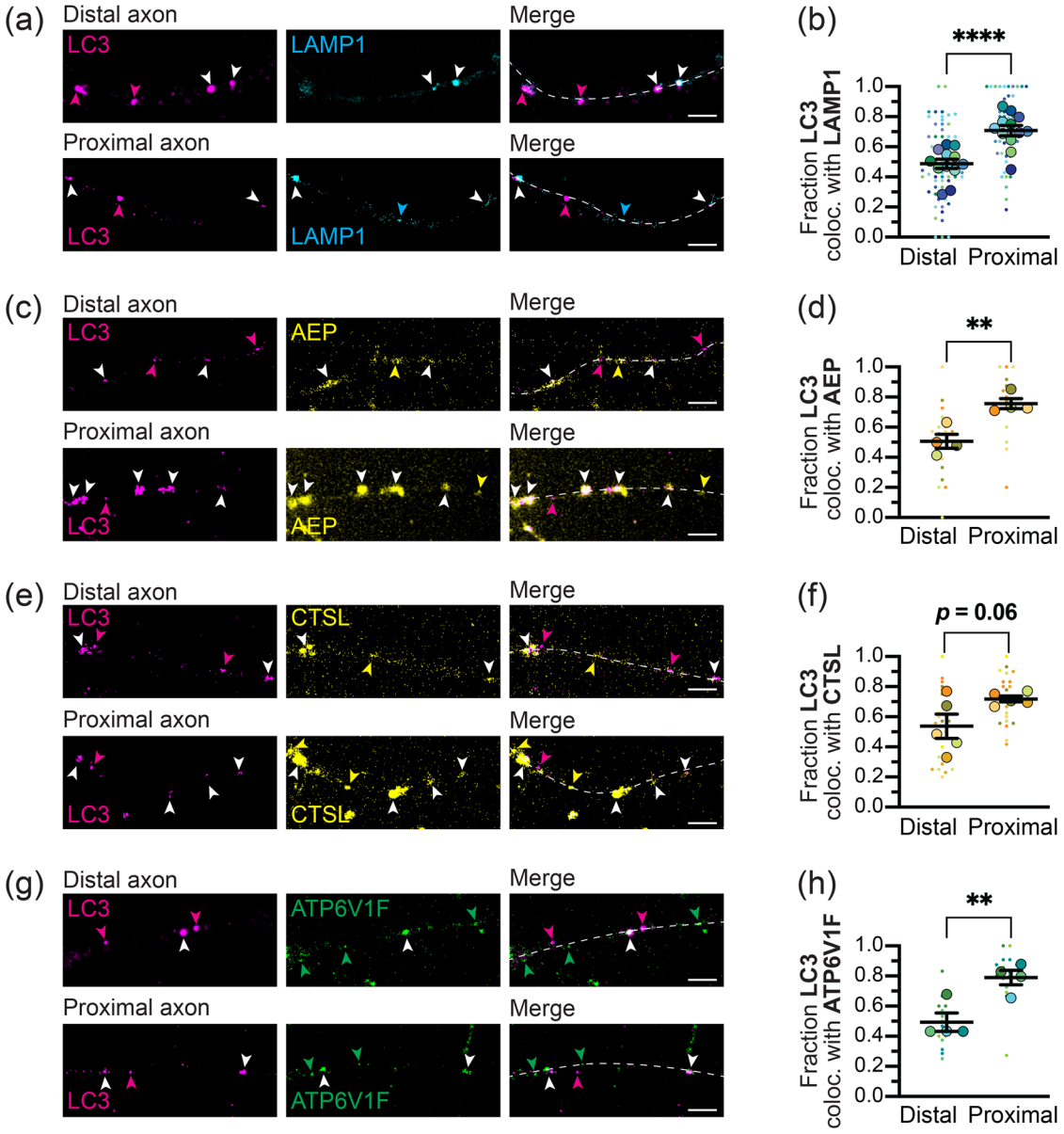

FIGURE 3: Spatial distribution of LC3 colocalization with lysosomal markers under endogenous conditions. Maximum projections (a) and quantification (b) showing LC3 and LAMP1 overlap in the distal and proximal axon. $n = 12$ trials; unpaired t test ($p < 0.0001$). Maximum projections (c) and quantification (d) showing LC3 and AEP overlap in the distal and proximal axon. $n = 4$ trials; unpaired t test ($p = 0.0045$). Maximum projections (e) and quantification (f) showing LC3 and CTSL overlap in the distal and proximal axon. $n = 5$ trials; unpaired t test ($p = 0.0605$). Maximum projections (g) and quantification (h) showing LC3 and ATP6V1F overlap in the distal and proximal axon. $n = 4$ trials; unpaired t test ($p = 0.0090$). Magenta arrows, LC3 alone; cyan/yellow/green arrows, respective lysosomal marker alone; white arrows, colocalization. Scale bar, 5 µm. Fractions are all over the total LC3 puncta in that region. Small dots throughout represent individual cells, while the larger outlined dot of the same color represents the mean from that trial. Statistics were performed using the means from the trials. Bars show mean ± SEM. Dashed line represents axon. ns, $p > 0.05$; *, $p < 0.05$; **, $p < 0.01$; ****, $p < 0.0001$.

labels acidified compartments and can therefore be used as a proxy for fusion with endolysosomes. In both the distal and mid-axonal regions, LysoTracker+ AVs were no more likely to exhibit retrograde motion than LysoTracker– AVs, implying that the motility switch is not connected to fusion (Figure 5, e and f). We therefore assume a single-constant switching rate regardless of whether an AV has fused with an endolysosome.

Given that our model assumes that AVs are produced at the distal tip, we would expect that most LC3+ puncta found in the mid- and proximal axon must have arrived there after undergoing the switch to a retrograde state. To account for the remaining stationary puncta observed in these regions, we assume that a processively retrograde AV can switch into a temporary paused state (density $S(x)$) with rate k_h^r and can resume its retrograde motion with rate k_w^r. This paused state effectively reduces the average velocity of AVs as they move down the axon. The model is insensitive to the absolute rates k_h^r and k_w^r. However, the ratio k_h^r/k_w^r sets the ratio for paused to retrograde AVs ($S(x)/R(x)$) throughout the

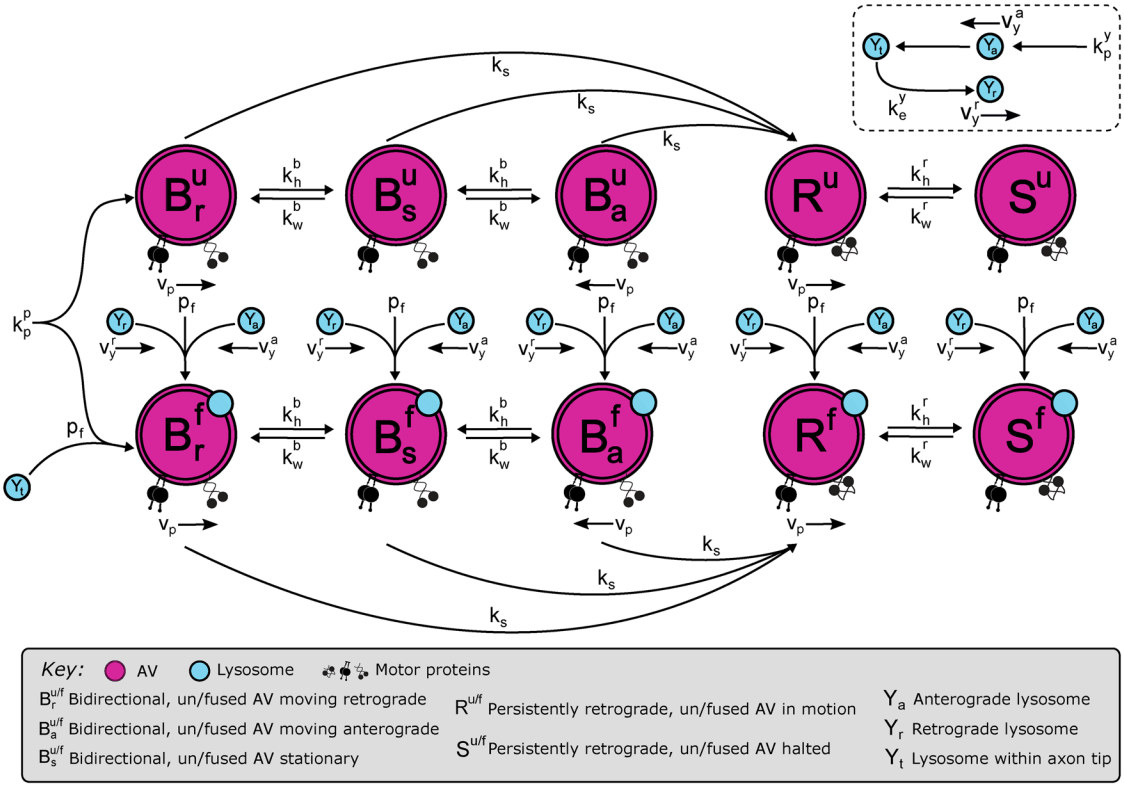

FIGURE 4: Mathematical model describes AV motility and endolysosome fusion as interconverting states. Magenta states indicate AVs, with top row corresponding to AVs that have not fused with an endolysosome and are bidirectional (B^u_a, B^u_r, B^u_s depending on current motion anterograde, retrograde, or stationary, respectively) or persistently retrograde (R_u: in motion, S_u: paused). Bottom row shows corresponding states for AVs that have fused with an endolysosome. Lysosome states (Y_a: anterograde, Y_r: retrograde, Y_t: tip localized) are shown in cyan. Transitions between states are marked by arrows, with the corresponding transition rates labeled. AVs are produced in the B^u_r state and can become immediately fused with lysosomes stationed at the tip (Y_t) before entering the domain.

mid- and proximal axon. The mean-field model is described by a set of steady-state equations for the spatial densities of AVs in each motility state, defined and solved as described in *Materials and Methods*.

We estimate the transport switching rate constants k_s, k^r_h/k^r_w by considering the fraction of AVs in the processively retrograde state in the distal and mid-axonal regions, respectively. Specifically, we compute the fraction of retrograde AVs among those in the distal region ($x < 250$ μm) of the linear domain, as a function of the switching rate k_s (Figure 5g), allowing extraction of an estimated switching rate $k_s \approx 0.03$ min^{-1}. We then adjust the pausing rate after the retrograde switch to match the experimentally observed mid-axon fraction retrograde of 60.2% (Figure 5g), setting the ratio $k^r_h/k^r_w \approx 0.66$.

The AV production rate is estimated by scaling the average total density of AVs in the distal region to match the experimentally measured value $\rho_p = 0.045 \pm 0.004$ μm^{-1} (Figure 1c). The fitted value ($k_p{}^p \approx 0.30$ min^{-1}; Figure 5h) is within the range previously reported in different neuronal cell types (0.12–0.6 min^{-1}) (Maday and Holzbaur, 2014).

The mathematical model predicts that the density of bidirectional autophagosomes should fall off with distance away from the distal tip. The length scale for this decrease depends on the rate k_s of switching into the processive retrograde state, as well as the stopping and restarting rates for bidirectional AVs. In Figure 5i we show that the model predictions are approximately consistent with the observed distal distributions of stationary and bidirectional AVs.

Model for autophagosome–lysosome fusion. To explore fusion behavior, the distribution of lysosomes needs to be incorporated into the model. We assume that lysosomes are produced in the soma ($x = L$) with rate k^y_p. Upon biogenesis, lysosomes enter the axon and move in the anterograde direction toward the axonal tip, at an effective average velocity of $v^a_y = 1.4$ μm/s (Boecker *et al.*, 2020). Lysosomes that reach the distal tip of the domain ($x = 0$) enter a halted state. From there, they have a constant rate k^y_e of exiting the distal tip and initiating retrograde motion toward the soma at an effective velocity of $v^r_y = 1.1$ μm/s (Figure 6a). The densities of anterograde and retrograde lysosomes are defined as $Y_a(x)$ and $Y_r(x)$, respectively. The halted state (Y_t) encompasses all lysosomes accumulated in the distal bud of the axon without resolving the precise spatial position within that distal bud.

We note that the number of potential interactions between an AV and the lysosomes accumulated in the distal bud depends on the specific motility model chosen to represent bidirectional motion. Alternate models for AV motility in the distal region (such as an effectively diffusive motion [Newby and Bressloff, 2010] or bidirectional movement without stopping) would result in more frequent return visits to the distal tip and hence more potential fusion events. Our inclusion of explicit anterograde, retrograde, and stationary states is in line with experimental measurements of distal AV motility (Figure 5).

We assume a constant probability of fusion p_f each time a (previously unfused) AV and a lysosomal particle pass each other. Upon fusion, the endolysosome disappears and the autophagosome is

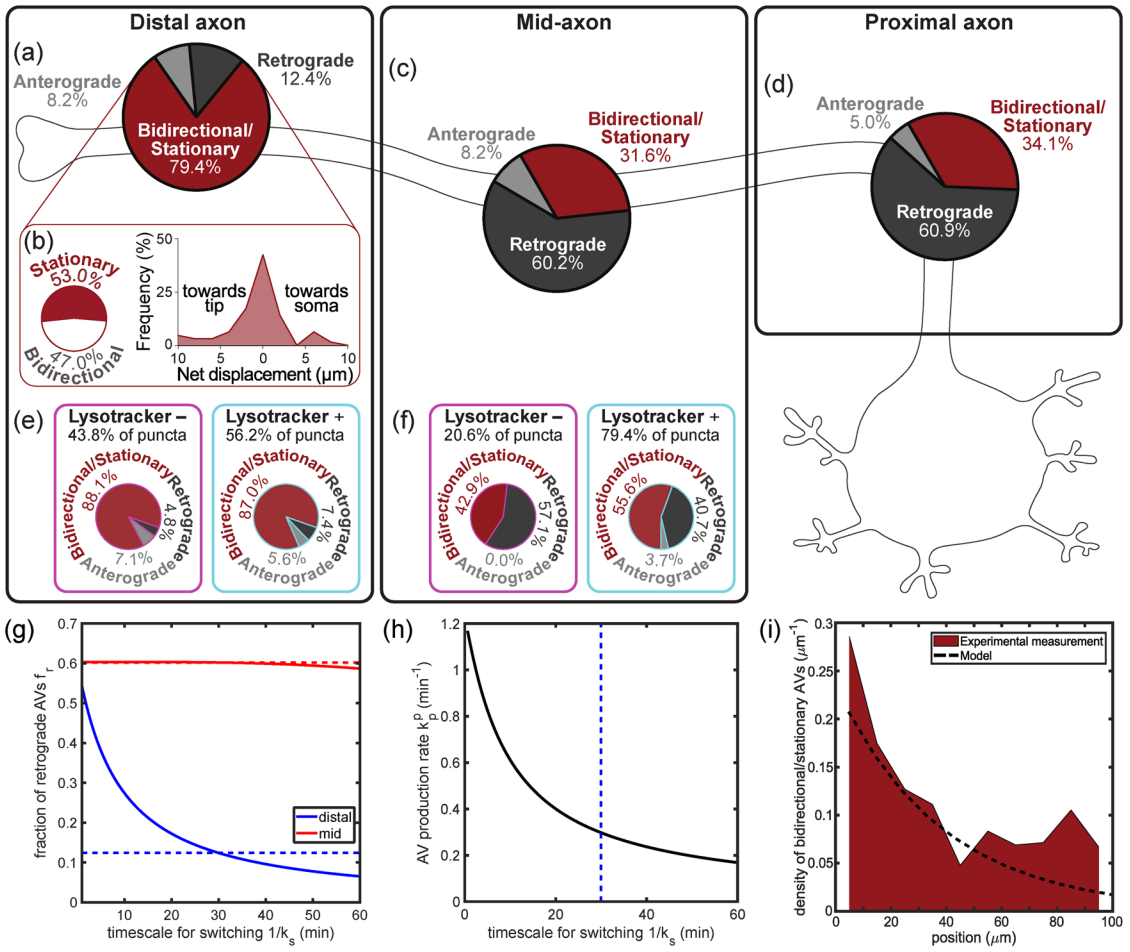

FIGURE 5: Production and motility switching rates determine spatial densities of bidirectional and retrograde AVs. (a) Motility of mCherry-LC3+ puncta in the distal axon ($n = 36$ cells). The majority of puncta exhibited limited motility (<10 μm net displacement over the course of a 1–3 min video), with <15% moving anterograde (≥10 μm toward the tip) or retrograde (≥10 μm toward the soma). (b) Among those puncta not undergoing long-range processive transport (from $n = 13$ cells), approximately half are classified as stationary, with an overall trajectory range <3 μm. The remaining puncta are classified as bidirectional. The displacement distribution among these puncta is approximately symmetric, indicating unbiased motion. (c, d) Motility states of mCherry-LC3+ puncta within the mid- (c, $n = 40$ cells) or proximal (d, $n = 35$ cells) axon. The majority of puncta exhibited retrograde (≥10 μm toward the soma) motility. (e, f) Motility states of mCherryLC3+ puncta within the distal (e) or mid- (f) axon, separated based on the fusion state determined by colocalization with LysoTracker. The retrograde-moving fractions (≥10 μm net displacement) among fused and unfused AVs were not significantly different within the distal ($n = 14$ cells, $p = 0.6933$, Fisher's exact test) or mid- ($n = 7$ cells, $p = 0.6722$, Fisher's exact test) axon. (g) From quantitative modeling, predicted fraction of AVs exhibiting retrograde motility within the distal (blue) and the mid-(red) axon, plotted against the timescale for switching ($\tau = 1/k$). The observed fractions within hippocampal axons are denoted by the corresponding dashed lines. (h) Model AV production rate k_p^p required to achieve the measured LC3+ density in the distal axon, plotted against the timescale for switching. The dashed line denotes the switching time obtained in panel g by fitting the retrograde fraction in the distal region. (i) Distribution of stationary/bidirectional AVs (with ≤10 μm net displacement) within the first 100 μm of the distal axon, obtained from live-cell imaging of the mCh-GFP-LC3 reporter ($n = 13$ cells, 62 AVs; bin width = 10 μm). The dashed black line denotes the distribution predicted by the mathematical model ($B_s + B_r + B_a + S$).

marked as fused. In our initial model, we assume that the ability of the AV to fuse with subsequent endolysosomes is lost after the initial fusion event. This is consistent with a model wherein the fusion machinery is inhibited following fusion (Saleeb *et al.*, 2019).

The mean-field equations describing the densities of lysosomes and unfused AVs are detailed in *Materials and Methods*. Their numerical solution allows us to calculate $F(x)$ (spatial density of puncta labeled with both LC3 and LAMP1) and $Y(x)$ (density of LAMP1+ puncta). We fitted three additional model parameters pertaining to fusion and lysosome behavior (p_f, k_p^y, k_e^y) by matching three different metrics to experimentally observed data: the average density of LAMP1+ puncta in the distal region ($\rho_y^{dist} \approx 0.07\ \mu m^{-1}$; Figure 1e), the fraction of AVs that have fused with a lysosome in the distal region ($f_f^{dist} \approx 0.5$) as measured by colocalization with LAMP1 (Figure 3b), and the ratio of LAMP1+ puncta to LC3+ puncta in the proximal region ($R^{prox} \approx 1.9$; Figure 1, c and e). The distal and proximal regions are defined as segments of length 250 μm from the distal and proximal ends of the domain, respectively. The distal lysosomal density also includes those lysosomes halted in the distal tip. Fitted parameter values are listed in Table 1.

The distal fraction fused f_f^{dist} is largely dependent on the fusion probability and the overall density of lysosomes in the distal region.

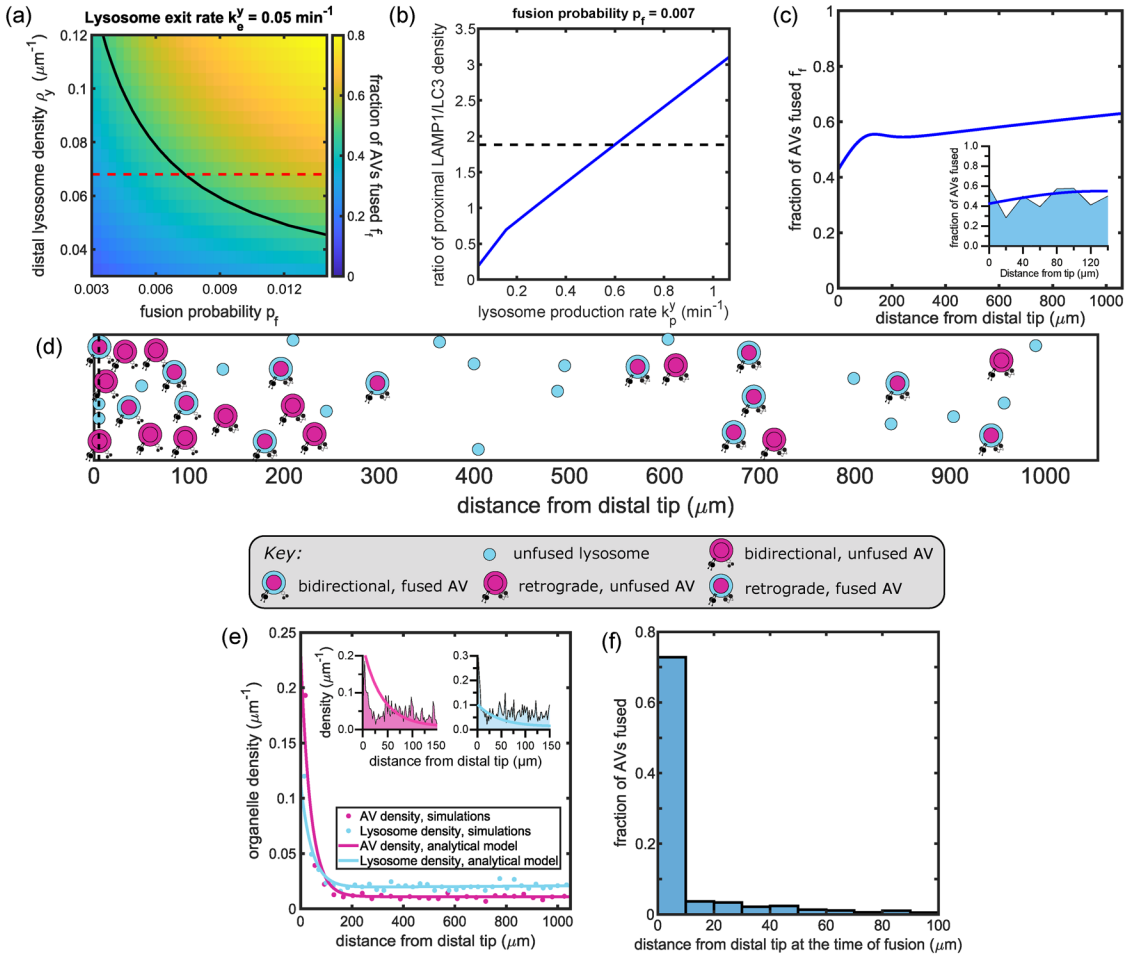

FIGURE 6: Model for AV–endolysosome interaction dynamics predicts spatial distributions of fused and unfused organelles. (a) Fraction of AVs fused within the distal axon f_f, plotted against the fusion probability p_f and the lysosome density in the distal region ρ_y. The tip-exit rate for lysosomes key is set to 0.05 per min. The solid black curve denotes the observed value of $f_f = 0.5$, based on LC3+ puncta colocalized with LAMP1+ puncta in the distal axon, tracing a contour line along the green color. The dashed red line denotes the observed density of LAMP1+ puncta in the distal axon. (b) The ratio of the linear density of lysosomes to AVs in the proximal axon, plotted against the lysosome production rate. The dashed black line denotes the measured value determined by enumerating LAMP1+ and LC3+ puncta in the proximal axon. (c) Spatial variation in the fraction of AVs fused at different positions along the axon. The inset zooms into the distal region, overlaid with the experimentally observed distribution. (d) Snapshot from agent-based simulation of organelle dynamics, after reaching steady state. Video of simulation is provided as Supplemental Video 1. For clarity, organelle size and axon cross-section (vertical axis) are not shown to scale. (e) The linear density of LC3+ puncta (magenta) and LAMP1+ puncta (cyan) along the axon. Solid lines are obtained from the mean-field model and dots from stochastic simulations. Insets show comparison to experimentally measured densities in distal region, from Figure 1, d and f. (f) Histogram of position at first fusion for individual AVs, extracted from simulated trajectories. Vertical axis is normalized to the overall number of AVs that undergo fusion before reaching the soma. The most distal 100 μm is shown.

We plot this metric in Figure 6a, showing that a unique, low value of the fusion probability $p_f \approx 0.007$ matches both observations of the distal lysosomal density and the fraction of fused AVs in the distal region. The relative density of lysosomes in the distal and proximal regions is determined by the balance between the lysosomal production rate and their retrograde exit rate from the distal tip. We therefore used the measured ratio of LAMP1+ to LC3+ puncta in the proximal axon to estimate the appropriate value for $k_p^y \approx 0.56$ min^{-1}.

Given the fitted model parameters, one key prediction is the spatial distribution of fused AVs. The fraction of AVs that have fused is plotted as a function of spatial position in Figure 6c. Notably, more than 40% of AVs are fused in the far distal tip (within the first few microns), and the fused fraction increases only slightly over the rest of the domain. This implies that of those AVs that fuse anywhere within the axon (~60% of the full population), more than two-thirds have already fused by the time they move away from the distal tip. The predicted flat curve for the fraction fused is consistent with experimental observations (Figure 6c, inset).

To further validate our mean-field model, we make use of stochastic simulations of lysosomal and AV particles in a linear domain (Figure 6d and Supplemental Video 1; see *Materials and Methods* for details). The spatial distributions of LC3+ and LAMP1+ particles are similar for both the stochastic simulations and the mean-field model (Figure 6e). The simulations further enable direct tracking of where in the domain each individual AV

Parameter	Description	Value	Reference
		Fixed parameters	
L	Length of the main axon	1055 μm	Supplemental Figure S2
v_p	AV velocity	0.75 μm/s	Boecker *et al.*, 2020
v_y^a	Lysosome velocity (anterograde)	1.3 μm/s	Boecker *et al.*, 2020
v_y^r	Lysosome velocity (retrograde)	1.1 μm/s	Boecker *et al.*, 2020
		Measurements	
ρ_p	Distal LC3 density	(0.045 ± 0.004) μm^{-1}	Figure 1c
ρ_y	Distal LAMP1 density	(0.068 ± 0.007) μm^{-1}	Figure 1e
R	Proximal LAMP1/LC3 ratio	1.88 ± 0.11	Figure 1, c and e
f_f	Distal fused AV fraction	0.49 ± 0.03	Figure 3b
f_r	Distal retrograde AV fraction	0.12 ± 0.02	Figure 5a
		Fitted parameters			
Parameter	**Description**	**Value (linear)**	**Reference**	**Value (branched)**	**Reference**
k_s	AV retrograde switch rate	0.03 min^{-1}	Figure 5g	0.03 min^{-1}	Figure 7b
k_h^r/k_w^r	Retrograde AV halt rate (scaled)	0.66	–	0.60	–
k_p^p	AV production rate	0.30 min^{-1}	Figure 5h	0.30 min^{-1}	Figure 7c
p_f	Fusion probability	0.007	Figure 6a	0.007	Figure 7d
k_p^y	Lysosome production rate	0.60 min^{-1}	Figure 6b	3.37 min^{-1}	Figure 7e
k_e^y	Lysosome tip exit rate	0.05 min^{-1}	Figure 6a	0.04 min^{-1}	Figure 7d

TABLE 1: Parameters for modeling organelle dynamics in autophagy.

becomes fused. This distribution of the position at first fusion (x_f) shows a strong peak at the distal tip (Figure 6f). Given our fitted model parameters, we expect most AVs to fuse either in the distal tip or very soon after exit from the tip, with a smaller broad tail in the distribution corresponding to those that fuse throughout the rest of the axon. We note that this is a prediction of the model, which assumes that fusion probability is constant regardless of position or motility state. The predominance of fusions in the far distal tip and their paucity in the mid- and proximal axon is a direct consequence of the observed organelle densities and motility patterns.

Another prediction of the basic model is that the overall density of AVs must fall off with distance from the distal tip, over a length scale of a few hundred micrometers. This is an inherent consequence of the assumption that AVs are produced in the distal tip and slowly transition to retrograde motility, with only 12% of the distal AVs observed to have made this switch. Because bidirectional organelles spread out slowly from their point of origin, these assumptions imply that the AVs must pile up in the distal region compared with elsewhere in the axon. A modest falloff in the density of LC3+ puncta is indeed observed within the distal region (Figure 6e, inset). However, the observed LC3+ density is similar in both the distal and proximal regions (Figure 1d). This observation is at odds with the prediction of the model that the proximal AV density should be only 24% of the distal density. One potential explanation for this discrepancy is the nonlinear geometry of the axon, with multiple distal tips potentially producing AVs that converge in the proximal region. We therefore expand our model to consider a branched axonal architecture.

Collateral branches supply AVs to maintain a broad axonal distribution. Neuronal axons form multiple branches known as axon collaterals. The generation of these collaterals enables a neuron to establish robust connectivity with neighboring targets and plays an important role in the development of the CNS (Gallo, 2011; Kalil and Dent, 2014). We find that primary hippocampal neurons at 7–10 days in vitro have an average of $n_c \approx 5$ axon collaterals per neuron with an average length of $L_c \approx 164$ μm (Supplemental Figure S2).

We extend our mean-field model to incorporate a branched geometry consisting of a single main axon along with five collaterals of length L_c placed at equispaced intervals along the mid-axon (Figure 7a). The end point of each collateral is assumed to be functionally equivalent to the main axon tip, producing AVs at a fixed rate k_p^p and allowing lysosomes to halt when they reach the distal tip, followed by returning at rate k_e^y in the anterograde direction. The mean-field densities for AVs and lysosomes obey the same steady-state equations as the linear model, with flux-conserving boundary conditions at the junctions (see *Materials and Methods*). The parameter values are again estimated by fitting to experimentally determined metrics (Figure 7, b–e). All the parameter estimates (Table 1) are similar to those in the linear model, except for the lysosome production rate. The branched model requires a lysosome production rate that is roughly sixfold higher than that of the linear model, enabling a similar density of lysosomes to reach each individual distal tip.

The predicted spatial densities of LC3 and LAMP1 puncta along the main axon are shown in Figure 7f. At each branch junction, the density of AVs increases as the retrograde organelles coming from the collateral join those moving along the main axon. The predicted average density of AVs in the proximal region is now approximately $\rho_p^{prox} \approx 0.06\ \mu m^{-1}$, slightly higher than the distal density and comparable to experimental measurements (Figure 1, c and d). We note that the experimental data (Figure 1f) indicate a gradual increase in lysosomal density within the most proximal region of the axon. This

increase is not reproduced by our simplified model, indicating the possibility that other features (such as, e.g., the actin-rich axon initial segment [Song *et al.*, 2009; Ozkan *et al.*, 2021]) may be causing increased halting or reversal of lysosomes in the far proximal zone.

The model with branched axon geometry also yields a relatively flat profile for the fraction of AVs that have fused with a lysosome (Figure 7g). While the distal fraction fused $f_f^{dist} = 0.5$ was used to fit the model parameters, the proximal fraction fused $f_f^{prox} = 0.73$ is a prediction of the model that approximately matches experimental measurements ($f_f^{prox} \approx 0.71 \pm 0.03$) (Figure 3b).

Modeling predicts that individual AVs undergo small numbers of fusion events. Our basic model for organelle distributions was developed under the assumption that each individual AV can fuse with at most one endolysosome. However, the actual number of fusion events between an autophagosome and lysosomes during transit along the axon is unknown. A variety of models could be conceived wherein the probability of fusion p_f decreases as a function of the number of fusions already undergone or over time following the initial fusion event. The "one-and-done" model proposed here constitutes an extreme case where this decrease is very steep so that each AV immediately becomes incapable of fusion after the first such event.

We also consider a model for the opposite limit, where the number of fusions is unlimited and the fusion probability remains constant, regardless of how many previous endolysosomes have fused into a given AV. This alternate model and its parameterization are detailed in the Supplemental Information (Section S3). In principle, such a model allows for a "snowball" effect where a single AV sweeps up large numbers of endolysosomes in successive fusions, leaving very few of them to reach the distal tips. However, given the fitted model parameters, we find that the average number of fusions accumulated by each AV is quite small: less than one in the distal axon and rising to two fusions by the time an AV reaches the soma (Figure 7g, red dots). This is a direct consequence of the low value of the fitted fusion probability $p_f \approx 0.007$, which also leads to the fraction of AV with at least one fusion being very similar in both the "one-and-done" and the "unlimited fusions" model (Figure 7g, blue curves). Thus, a typical AV will have passed an average of ≈270 lysosomes by the time it reaches the soma but will have fused with only a couple of them.

The available data described here do not allow us to distinguish whether there is a regulatory process that explicitly prevents an AV from fusing with multiple lysosomes. However, our quantitative model demonstrates that there cannot be a "snowball" effect wherein individual AVs sweep up large numbers of lysosomes in multiple fusion events. Instead, the observed organelle distributions imply that the average number of fusions per AV is quite low, with only a small fraction of AV–endolysosome passage events resulting in fusion and a large fraction of endolysosomes surviving to reach the distal tip of the axon.

Distal fusion with endolysosomes is followed by slow inner membrane degradation

The next step in AV maturation following fusion is acidification. AV acidification can be measured in live cells by colocalization with the dye LysoTracker, which labels acidified compartments. In primary hippocampal neurons, we find that about 60% of LC3+ puncta colabel with LysoTracker in the distal axon, with a slow increase to about 90% in the proximal axon (Figure 8a), consistent with published data examining colocalization between LC3 and LysoTracker, LAMP1/Rab7, and enzymatic activity sensors (MagicRed, MDW941) in multiple neuronal cell types (Supplemental Table S1). This reflects the early peak in fusion events and long tail observed in the modeling (Figure 6, c and f). By contrast, the dual-color LC3 reporter mCherry-EGFP-LC3 shows a different distribution of AV acidification. This reporter fluoresces in the red and green wavelengths in nonacidified environments but in only red in acidic environments due to the quenching of the EGFP moiety below pH 5.8 (Campbell and Choy, 2001; Pankiv *et al.*, 2007). Use of this reporter in primary hippocampal neurons revealed very few AVs in the distal axon showing acidity-triggered EGFP quenching (Figure 8a; Supplemental Figure S4, d–f). Furthermore, while all of the other lysosomal markers labeled the vast majority of AVs by the mid- or proximal axon, fewer than half of AVs in the proximal axon demonstrated EGFP quenching (Figure 8a). This is consistent with published data in iPSC-derived cortical neurons (Boecker *et al.*, 2021).

The double-membraned nature of AVs is key to reconciling these observations (Figure 8b). During biogenesis, the growing phagophore (Stage 0) engulfs cargo such that the cargo ends up inside the inner autophagosomal membrane (IAM), within the central lumen of the closed autophagosome (Stage I). When an autophagosome and endolysosome fuse, the endolysosomal membrane becomes part of the outer membrane and the contents of the endolysosomal lumen (e.g., degradative enzymes, H^+) are delivered into the intermembrane space, resulting in rapid acidification of that space (Stages II and III). In nonneuronal cells, LysoTracker has been shown to specifically localize to the intermembrane space and then collapse inward when the IAM is degraded (Tsuboyama *et al.*, 2016). Axonal AVs are condensed due to the narrow diameter of the axon and rarely appear as rings after leaving the tip, making this intermembrane space and inner membrane collapse difficult to resolve.

Once the IAM is broken down, the central lumen and the cargo therein are exposed to the acidic pH required to activate enzymatic degradation (Stage IV). Unlike LysoTracker and the fluorogenic enzyme activity sensors, the tandem mCherry-EGFP-LC3 marker localizes specifically to the inner lumen of the AV (Figure 8b). Initially LC3 localizes to both the inner and outer membranes, conjugated to the lipid phosphatidylethanolamine so that the protein extends into the lumen on the inner membrane and into the cytosol on the outer membrane (Martens and Fracchiolla, 2020). The protein extending into the cytosol is cleaved by the autophagy protease ATG4 (Kauffman *et al.*, 2018), leaving only the lumenal protein, and fluorophores, intact. Therefore quenching of the EGFP moiety can be used as a specific readout of IAM degradation, indicating the point at which the IAM breaks down and the lumenal LC3 and other cargo are exposed to the acidic pH (Figure 8b). A comparison of the tandem mCherry-EGFP-LC3 marker and other endolysosomal markers thus highlights two distinct steps in autophagic maturation: first, endolysosomal fusion enables acquisition of degradative enzymes and triggers acidification of the intermembrane space; second, breakdown of the IAM enables the enzymes and acidic environment to reach the lumen.

Several explanations could account for the spatial difference between AV–lysosome fusion and IAM degradation in hippocampal neurons. One possibility is that the endolysosomes in the distal region may be lacking the enzymes responsible for IAM degradation. However, we probed for the lysosomal lipase PLA2G15, thought to be responsible for IAM breakdown (Li *et al.*, 2022), and found essentially the same colocalization with LC3 and LAMP1 as with other lysosomal enzymes (Figure 8, c–f). We therefore conclude that the phospholipase required for IAM degradation is acquired in the initial AV–endolysosome fusion event.

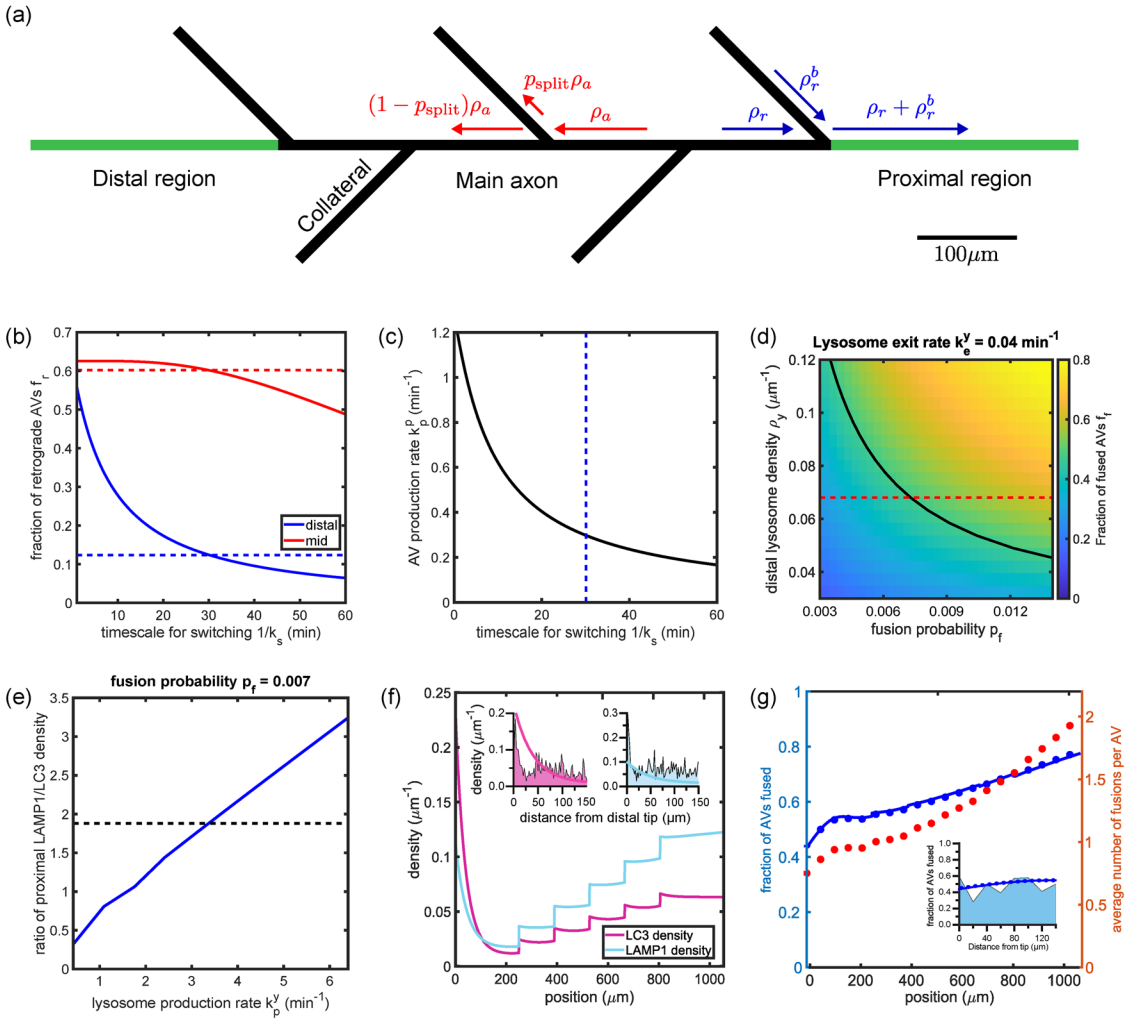

FIGURE 7: Mathematical model with branched axon morphology is consistent with measured organelle distributions. (a) Schematic of the branched axon geometry. All the distributions shown are within the main axon. Green sections indicate the extent of distal and proximal regions. Text in red and blue indicates the boundary conditions at branch junctions for anterograde and retrograde organelles, respectively. Scale bar, 100 μm. (b) Fraction of AVs exhibiting retrograde motility within the distal (blue) and the mid- (red) regions of the main axon, plotted against the timescale for switching. Observed fractions in hippocampal neurons are shown with corresponding dashed lines. (c) AV production rate k_p^p required to achieve the measured LC3+ density in the distal axon, plotted against the timescale for switching. The dashed line denotes the switching time obtained in panel b. (d) Fraction of AVs fused within the distal axon f_f plotted against the fusion probability p_f and the lysosome density in the distal region. The tip-exit rate for lysosomes key is set to 0.04 per min. The solid black line denotes measured value of f_f, based on LC3+ puncta colocalized with LAMP1+ puncta in the distal axon. The dashed red line denotes the density of LAMP1+ puncta observed in the distal axon. (e) The ratio of the lysosome density to AV density in the proximal axon, plotted against the lysosome production rate. Dashed black line denotes the measured value determined by enumerating LAMP1+ and LC3+ puncta in the proximal axon. (f) The linear density of LC3+ puncta (magenta) and LAMP1+ puncta (cyan) along the axon. The inset zooms into the distal region, showing the model prediction overlaid on experimentally observed LC3+ and LAMP1+ densities from Figure 1, d and f, respectively. (g) Spatial variation in the fraction of AVs fused at different positions along the axon. The solid blue line denotes the fraction fused in the base "one-and-done" model; blue markers give corresponding results for a modified model with unlimited fusion events (see Supplemental Figure S3). The inset zooms into the distal region, overlaid with the experimentally observed distribution. Red markers denote the average number of fusions per AV for the unlimited fusion model.

An alternative explanation for the different spatial profiles of AV–endolysosome fusion and IAM degradation is a temporal gap: slow kinetics of IAM degradation could allow time for the AVs to reach the soma before completion. We expand our parameterized one-and-done model for AV fusion in a branched axonal geometry (Figure 7) by introducing a single new parameter, k_d, describing a constant rate process for complete inner membrane degradation in an AV that begins after fusion with an endolysosome. The model is solved (see *Materials and Methods*) to compute the spatially resolved fraction of phagosomes $f_d(x)$ that have undergone full IAM decay. We estimate the degradation timescale $\tau_d = 1/k_d$ by considering the fraction of fully mature AVs in the distal, mid-, and proximal axonal regions. A single value of $\tau_d \approx 100$ min is consistent with the experimentally observed values in all three regions (Figure 8g).

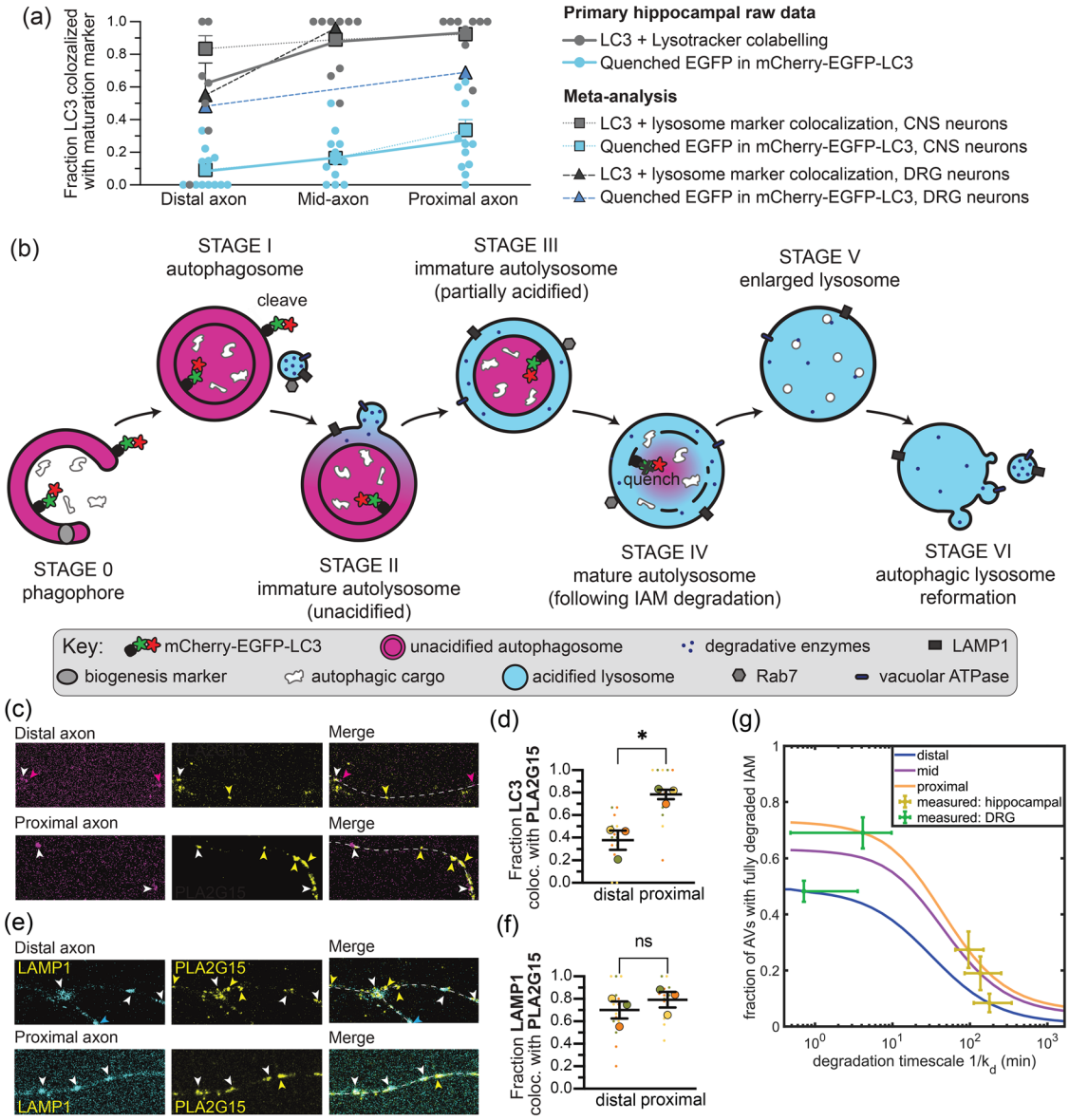

FIGURE 8: Distal fusion with endolysosomes is followed by slow inner membrane degradation. (a) Across studies and cell types, markers for AV–endolysosome fusion (LAMP1, Rab7, LysoTracker, MagicRed, MDW941) are acquired more distally than the GFP moiety of mCherry-GFP-LC3 quenches. Circular points represent primary hippocampal raw data, $n = 8$–12 axons. Lines represent quantities estimated from previous studies (see Supplemental Table S1). (b) When an AV fuses with an endolysosome, the endolysosome's contents enter the intermembrane space and its membrane proteins join the outer membrane. Following IAM degradation, the autophagic cargo, including mCherry-GFP-LC3, is exposed to lysosomal pH and proteases. Following degradation, the recyclable contents are exported and the remaining organelle is broken into smaller lysosomes. The rate of transition from fusion to membrane breakdown is denoted by k_d. (c) Maximum projections showing LC3 and phospholipase A2 group XV (PLA2G15) overlap in the distal and proximal axon. (d) Comparison of the total LC3+ puncta colocalized with PLA2G15 in the distal and proximal axon. $n = 3$ trials; unpaired t test ($p = 0.0127$). (e) Maximum projections showing LAMP1 and PLA2G15 overlap in the distal and proximal axon. (f) Comparison of the total LAMP1+ puncta colocalized with PLA2G15 in the distal and proximal axon. $n = 3$ trials; unpaired t test ($p = 0.4248$). Magenta arrows, LC3 alone; yellow arrows, PLA2G15 alone; cyan arrows, LAMP1 alone; white arrows, colocalization. Scale bar, 5 μm. Fractions are all over the total LC3+ or LAMP1+ puncta in that region. Small dots throughout represent individual cells, while the larger outlined dot of the same color represents the mean from that trial. Statistics were performed using the means from the trials. Bars show mean ± SEM. ns, $p > 0.05$; *, $p < 0.05$. (g) Modeled fraction of AVs with degraded inner membrane f_d plotted as a function of the degradation time ($\tau_d = 1/k_d$). Plots shown are averages over the most distal (blue) and most proximal (orange) 250 μm regions, along with the middle section (pink) of a modeled axon of length 1055 μm. Parameters used in the model are the same as those extracted from Figure 7. The degradation times corresponding to measured values of f_d in the distal, mid-axonal, and proximal regions are shown in yellow for hippocampal neurons and in green for DRGs.

The predicted IAM degradation timescale of ≈100 min is longer than the average time required for a newly formed AV to enter the processive retrograde state ($1/k_s \approx 30$ min) and to move from the distal tip to the soma ($L/v_p\,(1 + k_h^r/k_w^r) \approx 38$ min), accounting for the relatively small fraction of AVs whose IAM is degraded by the time they reach the soma. By comparison, the larger fraction of quenched EGFP in both the proximal and distal regions of dorsal root ganglia (DRG) neurons (Figure 8a; Supplemental Table S1) implies a much shorter IAM degradation timescale (Figure 8g), similar to that seen in mouse embryonic fibroblasts (Tsuboyama *et al.*, 2016).

DISCUSSION

This study provides a quantitative perspective on the maturation of neuronal autophagosomes, a key aspect of the autophagy pathway crucial to maintaining the recycling and turnover of cell components. Previous work showed that AVs form within the distal axon and then fuse with endolysosomes while moving toward the soma (Maday *et al.*, 2012; Stavoe *et al.*, 2016; Hill *et al.*, 2019). Fusion with endolysosomes is necessary for autophagic cargo degradation (Yin *et al.*, 2016), but the location and timing of fusion events and their relationship to AV maturation remained largely unclear.

We leveraged endogenous staining of AV and endolysosomal proteins to quantify the colocalization and spatial distribution of these organelles along the axons of primary rat hippocampal neurons, thereby avoiding potential overexpression artifacts. We find that LAMP1 colocalizes readily with both degradative hydrolases and active vATPase in both the distal and proximal axon (Figure 2), implying that LAMP1+ lysosomes are degradatively competent throughout the axon. We find that roughly half of AVs have fused with at least one competent endolysosome by the time they leave the distal axonal region (Figure 3). Live-cell imaging showed that most AVs in the distal axon are stationary or display short, unbiased bidirectional motions and that the majority of AVs in the mid- and proximal axon move retrograde toward the soma (Figure 5), consistent with previous studies (Maday *et al.*, 2012; Maday and Holzbaur, 2014; Cheng *et al.*, 2015; Boecker *et al.*, 2021; Cason *et al.*, 2021). Furthermore, we find that endolysosomal fusion is independent of retrograde transport initiation, with no difference in motility measurements between AVs with or without the endolysosomal marker LysoTracker (Figure 5, e and f).

While colocalization can indicate whether at least one fusion event has occurred, it cannot establish how many endolysosomes a single AV has fused with, or how many endolysosomes have passed without fusion. We therefore developed a mathematical model (Figure 4) to describe the motility and fusion interactions between AVs and endolysosomes, which allows us to translate the experimental measurements into a quantitative picture of the behavior of these organelles. Our model is parameterized against experimental metrics, including distal and proximal densities of AVs and endolysosomes, the fraction of fused AVs in the distal region, and the fraction of retrograde-moving AVs. The model shows that fusion of an AV with an endolysosome is expected to be a rare event, with <1% of passage events resulting in a fusion, and predicts that a large fraction of AVs will undergo their first fusion while still in the distal axon, with only a gradual increase in fusions thereafter (Figure 6).

Notably, we find that each AV is expected to fuse with only a few endolysosomes by the time it reaches the soma. The comparison between quantitative modeling and experimental data rules out the possibility of "snowball" AVs that soak up large numbers of endolysosomes while moving through the axon. This effect could be achieved by regulatory mechanisms that restrict subsequent fusions (Saleeb *et al.*, 2019) or as a result of the low probability of fusion upon passing (Saleeb *et al.*, 2019; Li *et al.*, 2020; Shen *et al.*, 2021). We hypothesize that the regulation of the SNARE protein syntaxin-17 (Stx17) may account for the relatively low number of fusion events predicted by the models (Itakura *et al.*, 2012). Stx17 is tightly regulated via posttranslational modifications, autoinhibition, and interaction with lysosomal membrane proteins to prevent ectopic fusion events (Saleeb *et al.*, 2019; Li *et al.*, 2020; Shen *et al.*, 2021). Regardless of the precise mechanism, the limited number of fusions allows for a broad distribution of endolysosomes throughout the axon.

An interesting feature that arises from the quantitative model is the interplay of motility and axonal geometry that determines the spatial distribution of organelles. High distal densities arise from the accumulation of stationary and bidirectional newly made AVs, enabling the majority of AVs to undergo fusion with an endolysosome while in the distal region. A branched axonal geometry allows AVs from multiple distal tips to converge in the proximal region, yielding a more uniform distribution of AVs across the entire main axon (Figure 7).

Fusion with an endolysosome is only the first step in the maturation of an AV. Our results show that nearly half of axonal AVs fuse with an endolysosome in the distal axon and exhibit concomitant partial acidification as marked by the pH-sensitive LysoTracker dye. However, only a small fraction of AVs become fully acidified, as indicated by the quenching of the EGFP moiety of mCherry-EGFP-LC3 in the AV lumen, by the time they reach the proximal axon (Figure 8a). These observations support a two-step model of autophagosome maturation, wherein fusion with an endolysosome allows for the acquisition of endolysosomal markers and acidification of the space between the outer and inner autophagosomal membrane (IAM), followed by the relatively slow degradation of the IAM (Tsuboyama *et al.*, 2016). It is only when the IAM is degraded that the AV lumen, including mCherry-EGFP-LC3 and the autophagic cargo, becomes fully acidified and cargo degradation may begin (Figure 8b). This model is consistent with data from multiple neuronal cell types, wherein acquisition of endolysosomal markers precedes quenching of the mCherry-EGFP-LC3 reporter (Supplemental Table S1; Figure 8a).

We incorporate the additional IAM degradation step into our model and extract a quantitative estimate of the rate for this process (Figure 8g) using mCherry-EGFP-LC3 quenching as a readout of IAM degradation. Notably, mCherry-EGFP-LC3 quenching is a marker for IAM degradation only if the mCherry-EGFP-LC3 proteins on the outer autophagosomal membrane, which extend into the cytosol, are cleaved. The protease ATG4 is responsible for cleaving LC3 and other members of its protein family from the outer autophagosomal membrane (Kauffman *et al.*, 2018). Given that ATG4s are also involved in autophagosome formation (Fujita *et al.*, 2008; Agrotis *et al.*, 2019), they are likely to be enriched in the distal axon, and therefore we anticipate that LC3 is rapidly cleaved from nascent autophagosomes in the distal axon. Furthermore, work in *Caenorhabditis elegans* neurons showed that ATG4 activity was required for autophagosome–lysosome fusion (Hill *et al.*, 2019); thus mCherry-EGFP-LC3 should be removed from the outer autophagosomal membrane before fusion with endolysosomes. Therefore we conclude that mCherry-EGFP-LC3 quenching is more likely a readout of IAM degradation rather than a readout of ATG4 activity.

We find that a single IAM degradation rate constant is consistent with the mCherry-EGFP-LC3 quenching measurements taken in both the distal and the proximal axon regions. The average IAM degradation time in primary hippocampal neurons ($\tau_d \approx 100$ min) is more than an order of magnitude longer than the time between fusion and IAM breakdown observed in mouse embryonic

fibroblasts (≈6.6 min) (Tsuboyama *et al.*, 2016). However, the rate extracted for DRG neurons (Figure 8g), derived from previously published data (Maday and Holzbaur, 2014), is relatively similar to that seen in mouse embryonic fibroblasts (Tsuboyama *et al.*, 2016). This highlights a difference not only between neurons and nonneuronal cells, but also between neuronal cell types that will need to be reconciled by future experimentation.

The modeling approach developed here serves as a framework for quantitatively understanding how the interplay between organelle transport and interactions across space and time governs autophagosome maturation. By combining modeling with direct measurements of organelle motility in live neurons and fusion under endogenous conditions, we have reconciled multiple conflicting studies of AV maturation and quantitatively connected organellar transport and fusion. Because autophagy defects are implicated in a variety of neurodegenerative diseases, obtaining a clear picture of this pathway is an important step toward a mechanistic understanding of such disorders.

MATERIALS AND METHODS

Primary hippocampal culture

Sprague Dawley rat hippocampal neurons at embryonic day 18 were obtained from the Neurons R Us Culture Service Center at the University of Pennsylvania. Cells (immunofluorescence, 180,000 cells; live imaging, 200,000 cells) were plated in 35 mm glass-bottom dishes (MatTek) that were precoated with 0.5 mg/ml poly-L-lysine (Sigma-Aldrich). Cells were initially plated in attachment media (MEM supplemented with 10% horse serum, 33 mM D-glucose, and 1 mM sodium pyruvate), which was replaced with maintenance media (neurobasal [Life Technologies] supplemented with 33 mM D-glucose, 2 mM GlutaMAX [Invitrogen], 100 U/ml penicillin, 100 mg/ml streptomycin, and 2% B-27 [ThermoFisher]) after 5–20 h. Neurons were maintained at 37°C in a 5% CO_2 incubator; cytosine arabinoside (Ara-C; final concentration 1 µM) was added the day after plating to prevent glia cell proliferation. Where applicable, neurons (5–7 days in vitro) were transfected with 0.35–1.5 µg of total plasmid DNA using Lipofectamine 2000 Transfection Reagent (ThermoFisher; 11668030) and incubated for 18–24 h.

iPSC-derived neuron culture

Induced pluripotent stem cells (iPSC) from the KOLF2.1J lineage were cultured, induced, and transfected exactly as described in (Pantazis *et al.*, 2021) with the following exception: to stably express doxycycline-inducible hNGN2 using a PiggyBac delivery system, iPSCs were transfected with the PB-TO-hNGN2 vector (gift from M. Ward, National Institutes of Health, Bethesda, MD) in a 1:2 ratio (transposase:vector) using Lipofectamine Stem (ThermoFisher); after 72 h, transfected iPSCs were selected for 48 h with 0.5 µg/ml puromycin (Takara).

Immunofluorescence experiments and analysis

Neurons were fixed at 7–10 days in vitro for 30 min at room temperature using Bouin's solution (Sigma-Aldrich; HT10132) supplemented with 8% sucrose and diluted 50% in maintenance media. Bouin's solution was then removed, and the cells were washed in phosphate-buffered saline (PBS) before being stored for up to 6 mo in PBS at 4°C. Cells were permeabilized for 8 min at –20°C in Optima Methanol (ThermoFisher; A456-1), washed in PBS, and then blocked for 1 h at room temperature in blocking solution (5% normal goat serum, 1% bovine serum albumin, 0.05% sodium azide). Primary and secondary antibodies (see Table 2 for manufacturers and dilutions) were diluted in blocking solution. Cells were incubated with diluted primary antibodies for 1 h at room temperature, followed by 3 × 5 min washes with PBS. Cells were then incubated with diluted secondary antibodies for 1 h at room temperature, followed by 3 × 5 min washes with PBS. Cells were mounted in Prolong Gold (ThermoFisher; P36930) and imaged within 48 h at 100× on a Perkin Elmer UltraView Vox spinning-disk confocal on a Nikon Eclipse Ti Microscope with a Plan Apochromat Lambda 60× 1.40 NA oil-immersion objective and a Hamamatsu EMCCD C9100-50 camera driven by Volocity (PerkinElmer). Z stacks were acquired in 0.1–0.2 µm steps.

Analysis was performed on maximum z projections in ImageJ (https://imagej.net/ImageJ2). Using the tau staining, axons were straightened (line width = 20 pixels) specifically in regions where they did not overlap with other cells. The straightened axon was then thresholded to create a mask wherein only the highest intensity gray values (0.5% for LC3 antibodies; 1% for all other antibodies) were counted as puncta, and any puncta ≤2 and >20 pixels in diameter were excluded. We considered other thresholds (Supplemental Figure S1c) and found that the thresholds selected here were a good fit with the puncta densities detected in previously published papers (Farfel-Becker *et al.*, 2019; Cason *et al.*, 2021) and in live cells (Supplemental Figure S1, e and f). Decreasing the threshold further (more stringent selection) yielded little difference in puncta densities (Supplemental Figure S1c). Furthermore, our focus is primarily on the spatial distribution of puncta and on comparative analysis of distal versus proximal regions (Supplemental Figure S1d). We therefore expect our results to be robust to the choice of threshold for puncta detection.

Puncta within 7 pixels (~1 µm) were considered colocalized. This colocalization threshold was selected because mammalian AVs are ≈1 µm in diameter and we were interested in quantifying colocalization to the same organelle, rather than colocalization of proteins within an organelle. Note that some immunofluorescence micrographs in the figures were prepared for presentation purposes only using the "Subtract background" feature in FIJI.

Live-cell neuron imaging and analysis

Where applicable, neurons were incubated with LysoTracker (25 nM) for 15–30 min, which was then removed for imaging. Neurons were imaged in imaging media (HibernateE [Brain Bits] supplemented with 2% B-27 and 33 mM D-glucose). Autophagosome behavior was monitored in the proximal (<250 µm from the soma), distal (<250 µm from the distal tip), or mid-axon of 7–8 days in vitro neurons imaged at a rate of 1 time point/s for 1–3 min. Neurons were imaged in an environmental chamber at 37°C with a Apochromat 100× 1.49 numerical aperture (NA) oil-immersion objective on the spinning-disk confocal described above. Only cells expressing moderate levels of fluorescent proteins were imaged to avoid overexpression artifacts or aggregation. It should be noted that the quality of the primary neuron dissections can affect autophagosomal motility, leading to variable retrograde fractions. Kymographs were generated in ImageJ using the MultiKymograph plug-in (line width = 5) and analyzed in ImageJ.

Puncta were identified based on their intensity (≥1.5 SDs above the mean background fluorescence) and duration in the video (≥5 s). Puncta were classified as either anterograde (moving ≥10 µm toward the axon tip), retrograde (moving ≥10 µm toward the soma), or stationary/bidirectional (net movement ≤10 µm during the video). Puncta that appear in the first or last 20 s of the video and drop out of the imaging window are counted as anterograde or retrograde if they are visible for <20 s and maintain a net velocity of ≥0.5 µm/s during that time; those whose net velocity is <0.5 µm/s are included in the stationary/bidirectional category.

Primary antibodies					
Target	**Host**	**Dilution**	**Manufacturer**	**Cat #**	**RRID**
LC3	Rabbit	1:250	Abcam	ab48394	AB_881433
LC3	Mouse	1:50	Santa Cruz	sc-376404	AB_11150489
LAMP1	Sheep	1:50–100	R&D Systems	AF4800	AB_1026176
LAMP1	Rat	1:50–100	DSHB	1d4b	AB_2134500
AEP	Sheep	1:100	R&D Systems	AF2058	AB_2234536
CTSL	Mouse	1:100	Novus	NB100-1775	AB_10124480
ATP6V1F	Mouse	1:100	Novus	NBP2-03498	AB_2904246
PLA2G15	Rabbit	1:125–150	Biorbyt	orb185108	AB_2904247
Tau	Chicken	1:300	Synaptic Systems	314 006	AB_2620049
Secondary antibodies					
Target	**Conjugation**	**Manufacturer**	**Cat #**	**RRID**	
Sheep	Alexa Fluor 405	1:1000	Abcam	ab175676	
Rat	Alexa Fluor 405	1:1000	Abcam	ab175671	
Chicken	Alexa Fluor 488	1:1000	ThermoFisher	A11039	
Rabbit	Alexa Fluor 555	1:1000	ThermoFisher	A21429	
Mouse	Alexa Fluor 555	1:1000	ThermoFisher	A21424	
Sheep	Alexa Fluor 594	1:1000	ThermoFisher	A11016	
Rabbit	Alexa Fluor 647	1:1000	ThermoFisher	A31573	
Mouse	Alexa Fluor 647	1:1000	ThermoFisher	A32728	
Methods for live-cell imaging					
Material			**Source**		
mCherry-EGFP-LC3			Gift from T. Johansen, University of Troms		
mScarlet-LC3B			Subcloned from Addgene #21073 and Addgene #85054		
LAMP1-mNeon			Subcloned from Addgene #98882 into PGK vector		
LysoTracker DeepRed			ThermoFisher Cat #L12492		

TABLE 2: Reagents used in the study.

Because fluorescent LC3 is cytosolic (as well as punctate) and neurites occasionally crossed in culture, raw videos were referenced throughout kymograph analysis. All comigration analyses were performed using kymographs.

Statistics for cell-based experiments

All statistical analyses were performed in Prism (GraphPad, San Diego, CA). Unless otherwise indicated, *n* indicates the number of trials (superplotting) wherein at least three cells were analyzed per trial. Neither parametricity nor preemptive sample-size (power) analyses were performed; however, data appear normally distributed and post hoc power calculations were used to confirm that a sufficient number of replicates were collected. Statistical measures are described in the legends.

Parameter estimates for bidirectional motility

We use live-cell dynamic imaging to extract estimates of the parameters describing AV bidirectional motility. Kymographs for LC3+ puncta within the distal 250 µm of the axon were obtained at a temporal resolution of 1 frame/s, for a total imaging period of 1–3 min. Manual tracing was used to extract a total of 49 AV trajectories from the kymographs. For these trajectories, the net displacement was used to classify AVs undergoing long-range retrograde motion (>10 µm toward the soma) or anterograde motion (>10 µm toward the tip), with the remaining particles classified as in a bidirectional/stationary state. Among the bidirectional/stationary particles, those whose trajectory showed a range (maximal minus minimal position) below 3 µm were classified as stationary and the rest as bidirectional. Among the bidirectional trajectories, we extracted all segments where the particles moved in a consistent direction (anterograde or retrograde) and found that the average displacement during such segments was $\lambda \approx 1.82 \pm 0.16$ µm, motivating our choice of a 2 µm run length in the model. This corresponds to a rate constant $k_h^b = v_p/\lambda \approx 0.4\ s^{-1}$ for transition into a stationary state. The restarting rate (k_w^b) is estimated according to the observed stationary fraction ($f_s \approx 53\%$; Figure 5b) as $k_w^b = k_h^b\,(1/f_s - 1) \approx 0.4\ s^{-1}$ Given the approximately symmetric histogram of displacements among stationary/bidirectional particles (Figure 5b), we assume that restarting rates and run length are identical in either direction for bidirectional motion.

Mean-field mathematical model for spatial distribution of AVs and endolysosomes

Densities of AVs in different motility states. The densities of AVs in different motility states on a linear domain can be described by the following set of equations:

$$\frac{dB_a}{dt} = v_p \frac{dB_a}{dx} - (k_s + k_h^b)B_a + \tfrac{1}{2}k_w^b B_s = 0 \tag{1a}$$

$$\frac{dB_r}{dt} = -v_p \frac{dB_r}{dx} - (k_s + k_h^b)B_r + \tfrac{1}{2}k_w^b B_s = 0 \tag{1b}$$

$$\frac{dB_s}{dt} = k_h(B_r + B_a) - (k_w + k_s)B_s = 0 \tag{1c}$$

$$\frac{dR}{dt} = -v_p \frac{dR}{dx} + k_s(B_r + B_a + B_s) - k_h^r R + k_w^r S = 0 \tag{1d}$$

$$\frac{dS}{dt} = k_h^r R - k_w^r S = 0 \tag{1e}$$

Each equation describes the time evolution of the organelle density in a particular motility state, including advective transport terms and reaction terms for interconversion between states. The time derivatives are set equal to zero as we focus on the time-independent, steady-state densities of AVs in the axon. The boundary conditions at the distal tip ($x = 0$) and soma ($x = L$) are given by

$$v_p B_r(0) = k_p^p + v_p B_a(0) \tag{2a}$$

$$B_a(L) = 0, \quad R(0) = 0 \tag{2b}$$

Here, the first equation sets equal the flux of outgoing retrograde AVs at the distal tip to the flux of incoming AVs (including a production term and returning anterograde organelles). The second two equations indicate that there are no anterograde AVs produced at the soma and no processively retrograde AVs produced at the distal tip, respectively. Equations 1 and 2 are solved using elementary matrix methods for a set of homogeneous first-order differential equations with constant coefficients on a linear interval (Boyce *et al.*, 2021).

We note that the kinetic parameters governing the bidirectional motion (k_h^b, k_w^b) serve to establish a quasi–steady-state distribution of AVs that are produced distally and spread away from the distal tip before switching into a processive retrograde state. Past theoretical work on intermittent bidirectional transport (Newby and Bressloff, 2009, 2010; Newby and Keener, 2011) showed that such dynamics can be modeled as an effective diffusion and drift under the quasi–steady-state assumption, thereby reducing the number of equations and states, while introducing a second-order differential equation. In the current case, the linear Eqs. 1 are sufficiently simple to solve that it was not necessary to invoke this simplification. Furthermore, AVs are known to engage in short bidirectional runs (Fu *et al.*, 2014), making the current model more biophysically realistic. Importantly, the detailed states of bidirectional motion affect the frequency of returns for AVs to the distal tips and hence the frequency of interaction with the lysosomes accumulated there.

Spatial densities of lysosomes and AV fusion states. The distribution of endolysosomes, as well as the different fusion states of the autophagic vesicles, depends on the fusion probability p_f between each pair of passing organelles. We note that the mean-field flux of lysosomes past a given autophagosome is given by the relative velocity of the two organelles multiplied by the lysosomal density. For instance, the overall flux of anterograde lysosomes moving past an anterograde AV is given by $|v_y^a - v_p|Y_a$. The rate of fusion events in each spatial position scales with this flux multiplied by the fusion probability p_f. We therefore write the following set of equations for the steady-state densities of unfused AVs in each motility state:

$$\frac{dB_a^u}{dt} = v_p \frac{dB_a^u}{dx} - \left(k_s + k_h^b + p_f\,|\,v_y^a - v_p\,|\,Y_a + p_f(v_p + v_y^r)Y_r\right)B_a^u + \frac{1}{2}k_w^b B_s^u = 0 \tag{3a}$$

$$\frac{dB_r^u}{dt} = -v_p \frac{dB_r^u}{dx} - \left(k_s + k_h^b + p_f(v_p + v_y^a)Y_a + p_f\,|\,v_y^r - v_p\,|\,Y_r\right)B_r^u + \frac{1}{2}k_w^b B_s^u = 0 \tag{3b}$$

$$\frac{dB_s^u}{dt} = k_h^b\left(B_r^u + B_a^u\right) - \left(k_w^b + k_s + p_f v_y^a Y_a + p_f v_y^r Y_r\right)B_s^u = 0 \tag{3c}$$

$$\frac{dR^u}{dt} = -v_p \frac{dR^u}{dx} + k_s(B_a^u + B_r^u + B_s^u) - \left(p_f(v_p + v_y^a)Y_a + p_f\,|\,v_y^r - v_p\,|\,Y_r\right)R^u - k_h^r R^u + k_w^r S^u = 0 \tag{3d}$$

$$\frac{dS^u}{dt} = k_h^r R^u - \left(k_w^r + p_f v_y^a Y_a + p_f v_y^r Y_r\right)S^u = 0 \tag{3e}$$

These densities correspond to puncta that are LC3+ but lack the LAMP1 endolysosomal marker in the bidirectional states (B_u^r, B_u^a, B_u^s for those moving retrograde, anterograde, and stationary, respectively), in a processive retrograde state (R^u), and in a paused state S^u.

The steady-state equations for anterograde (Y_a) and retrograde (Y_r) lysosome densities, as well as the number of lysosomes halted at the distal tip (Y_t), are given by

$$\frac{dY_a}{dt} = v_y^a \frac{dY_a}{dx} - p_f\left(|\,v_y^a - v_p\,|\,B_a^u + (v_p + v_y^a)(B_r^u + R^u) + v_y^a(B_s^u + S^u)\right)Y_a = 0 \tag{4a}$$

$$\frac{dY_r}{dt} = -v_y^r \frac{dY_r}{dx} - p_f\left((v_p + v_y^r)B_a^u + |\,v_y^r - v_p\,|\,(B_a^u + R^u) + v_y^r(B_s^u + S^u)\right)Y_r = 0 \tag{4b}$$

$$\frac{dY_t}{dt} = v_y^a Y_a(0) - k_e^y Y_t - p_f(v_p B_a^u(0) + k_p^p)Y_t = 0 \tag{4c}$$

In this basic model, it is assumed that each AV can fuse with at most one endolysosome, so that only the unfused organelles contribute to the terms describing the disappearance of lysosomes due to fusion.

The boundary conditions for Eqs. 3 and 4 are as follows:

$$v_p B_r^u(0) = (1 - p_f Y_t)\left(k_p^p + v_p B_a^u(0)\right) \tag{5a}$$

$$R^u(0) = 0, \quad v_y^r Y_r(0) = k_e^y Y_t \tag{5b}$$

$$B_a^u(L) = 0 \quad v_y^a Y_a(L) = k_p^y \tag{5c}$$

The right-hand side of Eq. 5a describes the flux of unfused AVs incoming to the distal tip (including production and anterograde return) multiplied by the probability that an AV fails to fuse with a lysosome stationed in the distal bud. This quantity is set equal to the flux of unfused retrograde AVs that leave the distal tip. Equation 5b sets equal the rate at which lysosomes stationed in the bud become motile again ($k_e^y Y_t$) and the flux of departing retrograde lysosomes ($v_y^r Y_r(0)$), thereby enforcing a steady-state value for the

number of lysosomes that can accumulate in the bud. Equation 5c defines the flux of anterograde lysosomes entering the domain from the soma to be equal to their production rate. The steady-state distributions for fused AVs can be obtained by subtracting the unfused AV densities (Eqs 3–5) from the total AV densities (Eqs. 1 and 2):

$$B_a^f = B_a - B_a^u, \quad B_r^f = B_r - B_r^u, \quad B_s^f = B_s - B_s^u, \quad R^f = R - R^u, \quad S^f = S - S^u \tag{6}$$

To solve for the steady-state distributions of unfused AVs and endolysosomes (Eqs. 3–5), we used the built-in solver bvp4c in Matlab (The MathWorks Inc, Natick, MA), which provides a 4th-order method for solving boundary value problems on a set of linear regions. Code for implementing the model for a given set of parameters is provided at https://github.com/lenafabr/autophagyTransportModel.

Model on branched geometry. On a branched axon geometry, the model equations (Eqs. 1, 3, and 4) remain the same as for the linear model, within each branch and each contiguous segment of the main axon. Boundary conditions for the distal tips (Eqs. 2 and 5) are assumed to be identical for the main axon tip and for the tips of all collaterals.

Additional boundary conditions at the collateral junctions are given by

$$\rho_r^{(m)}(l_m) + \rho_r^b(l_b) = \rho_r^{(m+1)}(0) \tag{7a}$$

$$\rho_a^{(m)}(l_m) = p_{\text{split}}\rho_a^{(m+1)}(0)$$

$$\rho_a^{(b)}(l_b) = (1 - p_{\text{split}})\rho_a^{(m+1)}(0) \tag{7b}$$

where $\rho_r^{(m)}$ and $\rho_r^{(b)}$ denote densities of retrograde organelles (B_r, R, Y_r) on a main axon segment and on a branch, respectively; $\rho_a^{(m)}$ and $\rho_a^{(b)}$ denote densities of anterograde organelles (B_a, Y_a), and l_m, l_b are the length of the corresponding main segment and branch. These equations set equal the steady-state flux of organelles approaching a junction (in the retrograde and anterograde directions) and the flux leaving that junction, preventing any accumulation of organelles at the junction over time.

We are not aware of any preexisting studies on how anterograde-moving organelles split between the main axon and the collateral when passing a junction point. In our model, we make the relatively simple assumption that anterograde organelles split in proportion to the number of distal tips downstream of the junction ($p_{\text{split}} = 1/(b + 1)$); that is, the chances of entering the collateral are 1/2 at the most distal junction, 1/3 at the second-to-last junction, and so forth. This approach allows similar numbers of organelles to reach each distal tip in the absence of fusion.

Steady-state solutions for IAM degradation model. We define the density $B_a^i = B_a - B_a^u - B_a^d$, for AVs in the bidirectional anterograde state that have fused with an endolysosome but have not yet undergone full IAM degradation. Analogous densities are defined for the other motility states (B_r^i, B_s^i, R^i, S^i).

The equations for these fused AVs with intact IAM, at steady state, are given by

$$\frac{dB_a^i}{dt} = v_p\frac{dB_a^i}{dx} - (k_s + k_h^b + k_d)B_a^i + p_f\left(|\, v_y^a - v_p \,|\, Y_a + (v_p + v_y^r)Y_r\right)B_a^u + \frac{1}{2}k_w^b B_s^i = 0 \tag{8a}$$

$$\frac{dB_r^i}{dt} = -v_p\frac{dB_r^i}{dx} - (k_s + k_h^b + k_d)B_r^i + p_f\left((v_p + v_y^a)Y_a + |\, v_y^r - v_p \,|\, Y_r\right)B_r^u + \frac{1}{2}k_w^b B_s^i = 0 \tag{8b}$$

$$\frac{dB_s^i}{dt} = k_h^b\left(B_r^i + B_a^i\right) - (k_w^b + k_s + k_d)B_s^i + p_f(v_y^a Y_a + p_f v_y^r Y_r)B_s^u = 0 \tag{8c}$$

$$\frac{dR^i}{dt} = -v_p\frac{dR^i}{dx} + k_s(B_a^i + B_r^i + B_s^i) - (k_h^r + k_d)R^i + p_f\left((v_p + v_y^a)Y_a + |\, v_y^r - v_p \,|\, Y_r\right)R^u + k_w^r S^i = 0 \tag{8d}$$

$$\frac{dS^i}{dt} = k_h^r R^i - (k_w^r + k_d)S^i + p_f\left(v_y^a Y_a + v_y^r Y_r\right)S^u = 0 \tag{8e}$$

$$v_p B_r^i(0) = p_f Y_t\left(k_p^p + v_p B_a^u(0)\right) + v_p B_a^i(0), \quad B_a^i(L) = 0, \quad R^i(0) = 0 \tag{8f}$$

Agent-based stochastic simulations for interacting organelles

Organelle transport interactions are simulated explicitly using custom-written FORTRAN 90 code available at https://github.com/lenafabr/particleDynamics1D. The agent-based simulation includes the same motile states and interactions as described in the mean-field model (Figure 4). We simulate a linear domain ($0 < x < L$) of length $L = 1055$ μm with $x = 0$ denoting the distal axonal tip and $x = L$ representing the soma. Point-particle endolysosomes spawn at the soma ($x = L$) and move toward the distal tip with a velocity v_y^a. Upon reaching the distal end, the endolysosomes halt at the tip before engaging in retrograde motility at a rate k_e^y with a velocity v_y^r. Point-particle AVs spawn at the distal tip ($x = 0$) in a bidirectional state moving in the retrograde direction. Motile AVs in the bidirectional state can halt with a rate k_h^b. Halted AVs resume motion at rate k_w^b, equally likely in the retrograde or anterograde direction. AVs from all bidirectional states can switch to processive retrograde state at a rate k_s. All motile AVs move at a velocity v_p and have a rate k_h^r for pausing and a rate k_w^r for restarting motility.

Interactions between an endolysosome and an AV occur whenever the two point-like organelles cross past each other. As the organelles move processively, an interaction is defined as any passage event where the order of the organelle positions along the axon is switched during a given time-step. Each such passage event results in fusion with a probability p_f. A fusion event destroys the lysosome, while the AV particle is marked as fused. The system is initialized with no particles and is evolved forward in time steps of $\delta t = 0.14$ s for a total time of 4×10^4 s, which is equivalent to 30 L/v_p and assumed to be sufficient to reach steady state. At each time step, the particles step in the appropriate direction a distance $v\delta t$ (where v is the corresponding particle velocity) and undergo a transition event with probability $1 - e^{-k\delta t}$ (where k is the rate for that particular state transition). The possible transition events and their rates are the same as those for the mean-field model (Figure 4).

ACKNOWLEDGMENTS

This research was supported by National Institutes of Health grant R01 NS060698 to E.L.F.H., a National Science Foundation (NSF) Graduate Research Fellowship (DGE-1845298) to S.E.C., a NSF CAREER grant (1848057) to E.F.K., and a Cottrell Scholar Award to

E.F.K. We thank Andrea Stavoe, Alex Boecker, Dan Dou, Anamika Agrawal, and Keaton Holt for insights and discussions.

REFERENCES

Agrawal A, Koslover EF (2021). Optimizing mitochondrial maintenance in extended neuronal projections. PLoS Comput Biol 17, e1009073.

Agrotis A, Pengo N, Burden JJ, Ketteler R (2019). Redundancy of human ATG4 protease isoforms in autophagy and LC3/GABARAP processing revealed in cells. Autophagy 15, 976–997.

Boecker CA, Goldsmith J, Dou D, Cajka GG, Holzbaur ELF (2021). Increased LRRK2 kinase activity alters neuronal autophagy by disrupting the axonal transport of autophagosomes. Curr Biol 31, 2140–2154.e2146.

Boecker CA, Olenick MA, Gallagher ER, Ward ME, Holzbaur ELF (2020). ToolBox: live imaging of intracellular organelle transport in induced pluripotent stem cell-derived neurons. Traffic 21, 138–155.

Boyce WE, DiPrima RC, Meade DB (2021). Elementary Differential Equations and Boundary Value Problems. Hoboken, NJ: John Wiley & Sons.

Campbell TN, Choy FY (2001). The effect of pH on green fluorescent protein: a brief review. Mol Biol Today 2, 1–4.

Canty JT, Yildiz A (2020). Activation and regulation of cytoplasmic dynein. Trends Biochem Sci 45, 440–453.

Cason SE, Carman PJ, Van Duyne C, Goldsmith J, Dominguez R, Holzbaur ELF (2021). Sequential dynein effectors regulate axonal autophagosome motility in a maturation-dependent pathway. J Cell Biol 220, e202010179.

Cheng XT, Xie YX, Zhou B, Huang N, Farfel-Becker T, Sheng ZH (2018). Characterization of LAMP1-labeled nondegradative lysosomal and endocytic compartments in neurons. J Cell Biol 217, 3127–3139.

Cheng XT, Zhou B, Lin MY, Cai Q, Sheng ZH (2015). Axonal autophagosomes recruit dynein for retrograde transport through fusion with late endosomes. J Cell Biol 209, 377–386.

Farfel-Becker T, Roney JC, Cheng XT, Li S, Cuddy SR, Sheng ZH (2019). Neuronal soma-derived degradative lysosomes are continuously delivered to distal axons to maintain local degradation capacity. Cell Rep 28, 51–64.e54.

Ferguson SM (2018). Axonal transport and maturation of lysosomes. Curr Opin Neurobiol 51, 45–51.

Fu MM, Nirschl JJ, Holzbaur ELF (2014). LC3 binding to the scaffolding protein JIP1 regulates processive dynein-driven transport of autophagosomes. Dev Cell 29, 577–590.

Fujita N, Hayashi-Nishino M, Fukumoto H, Omori H, Yamamoto A, Noda T, Yoshimori T (2008). An Atg4B mutant hampers the lipidation of LC3 paralogues and causes defects in autophagosome closure. Mol Biol Cell 19, 4651–4659.

Gallo G (2011). The cytoskeletal and signaling mechanisms of axon collateral branching. Dev Neurobiol 71, 201–220.

Goldsmith J, Ordureau A, Harper JW, Holzbaur ELF (2022). Brain-derived autophagosome profiling reveals the engulfment of nucleoid-enriched mitochondrial fragments by basal autophagy in neurons. Neuron 110, 967–976.e968.

Gowrishankar S, Yuan P, Wu Y, Schrag M, Paradise S, Grutzendler J, De Camilli P, Ferguson SM (2015). Massive accumulation of luminal protease-deficient axonal lysosomes at Alzheimer's disease amyloid plaques. Proc Natl Acad Sci USA 112, E3699–E3708.

Hancock WO (2014). Bidirectional cargo transport: moving beyond tug of war. Nat Rev Mol Cell Biol 15, 615–628.

Hara T, Nakamura K, Matsui M, Yamamoto A, Nakahara Y, Suzuki-Migishima R, Yokoyama M, Mishima K, Saito I, Okano H, Mizushima N (2006). Suppression of basal autophagy in neural cells causes neurodegenerative disease in mice. Nature 441, 885–889.

Hill SE, Kauffman KJ, Krout M, Richmond JE, Melia TJ, Colon-Ramos DA (2019). Maturation and clearance of autophagosomes in neurons depends on a specific cysteine protease isoform, ATG-4.2. Dev Cell 49, 251–266.e8.

Itakura E, Kishi-Itakura C, Mizushima N (2012). The hairpin-type tail-anchored SNARE syntaxin 17 targets to autophagosomes for fusion with endosomes/lysosomes. Cell 151, 1256–1269.

Johnson DE, Ostrowski P, Jaumouille V, Grinstein S (2016). The position of lysosomes within the cell determines their luminal pH. J Cell Biol 212, 677–692.

Kalil K, Dent EW (2014). Branch management: mechanisms of axon branching in the developing vertebrate CNS. Nat Rev Neurosci 15, 7–18.

Kauffman KJ, Yu S, Jin J, Mugo B, Nguyen N, O'Brien A, Nag S, Lystad AH, Melia TJ (2018). Delipidation of mammalian Atg8-family proteins by each of the four ATG4 proteases. Autophagy 14, 992–1010.

Koltun B, Ironi S, Gershoni-Emek N, Barrera I, Hleihil M, Nanguneri S, Sasmal R, Agasti SS, Nair D, Rosenblum K (2020). Measuring mRNA translation in neuronal processes and somata by tRNA-FRET. Nucleic Acids Res 48, e32.

Komatsu M, Waguri S, Chiba T, Murata S, Iwata J, Tanida I, Ueno T, Koike M, Uchiyama Y, Kominami E, Tanaka K (2006). Loss of autophagy in the central nervous system causes neurodegeneration in mice. Nature 441, 880–884.

Lee S, Sato Y, Nixon RA (2011). Lysosomal proteolysis inhibition selectively disrupts axonal transport of degradative organelles and causes an Alzheimer's-like axonal dystrophy. J Neurosci 31, 7817–7830.

Li Y, Cheng X, Li M, Wang Y, Fu T, Zhou Z, Wang Y, Gong X, Xu X, Liu J, Pan L (2020). Decoding three distinct states of the Syntaxin17 SNARE motif in mediating autophagosome-lysosome fusion. Proc Natl Acad Sci USA 117, 21391–21402.

Li Y, Wang X, Li M, Yang C, Wang X (2022). M05B5.4 (lysosomal phospholipase A2) promotes disintegration of autophagic vesicles to maintain C. elegans development. Autophagy 18, 595–607.

Lie PPY, Yang DS, Stavrides P, Goulbourne CN, Zheng P, Mohan PS, Cataldo AM, Nixon RA (2021). Post-Golgi carriers, not lysosomes, confer lysosomal properties to pre-degradative organelles in normal and dystrophic axons. Cell Rep 35, 109034.

Ma X, Godar RJ, Liu H, Diwan A (2012). Enhancing lysosome biogenesis attenuates BNIP3-induced cardiomyocyte death. Autophagy 8, 297–309.

Maday S, Holzbaur EL (2014). Autophagosome biogenesis in primary neurons follows an ordered and spatially regulated pathway. Dev Cell 30, 71–85.

Maday S, Wallace KE, Holzbaur EL (2012). Autophagosomes initiate distally and mature during transport toward the cell soma in primary neurons. J Cell Biol 196, 407–417.

Martens S, Fracchiolla D (2020). Activation and targeting of ATG8 protein lipidation. Cell Discov 6, 23.

Misgeld T, Schwarz TL (2017). Mitostasis in neurons: maintaining mitochondria in an extended cellular architecture. Neuron 96, 651–666.

Mogre SS, Christensen JR, Niman CS, Reck-Peterson SL, Koslover EF (2020). Hitching a ride: mechanics of transport initiation through linker-mediated hitchhiking. Biophys J 118, 1357–1369.

Mogre SS, Christensen JR, Reck-Peterson SL, Koslover EF (2021). Optimizing microtubule arrangements for rapid cargo capture. Biophys J 120, 4918–4931.

Mogre SS, Koslover EF (2018). Multimodal transport and dispersion of organelles in narrow tubular cells. Phys Rev E 97, 042402.

Newby JM, Bressloff PC (2009). Directed intermittent search for a hidden target on a dendritic tree. Phys Rev E 80, 021913.

Newby JM, Bressloff PC (2010). Quasi-steady state reduction of molecular motor-based models of directed intermittent search. Bull Math Biol 72, 1840–1866.

Newby JM, Keener JP (2011). An asymptomatic analysis of the spatially inhomogeneous velocity-jump process. Multiscale Modeling and Simulation 9, 735–765.

Ozkan N, Koppers M, van Soest I, van Harten A, Jurriens D, Liv N, Klumperman J, Kapitein LC, Hoogenraad CC, Farias GG (2021). ER–lysosome contacts at a pre-axonal region regulate axonal lysosome availability. Nat Commun 12, 4493.

Pankiv S, Clausen TH, Lamark T, Brech A, Bruun JA, Outzen H, Overvatn A, Bjorkoy G, Johansen T (2007). p62/SQSTM1 binds directly to Atg8/LC3 to facilitate degradation of ubiquitinated protein aggregates by autophagy. J Biol Chem 282, 24131–24145.

Pantazis CB, Yang A, Lara E, McDonough JA, Blauwendraat C, Peng L, Oguro H, Zou J, Sebesta D, Pratt G, *et al*. (2021). A reference induced pluripotent stem cell line for large-scale collaborative studies. bioRxiv, 472643.

Roney JC, Li S, Farfel-Becker T, Huang N, Sun T, Xie Y, Cheng XT, Lin MY, Platt FM, Sheng ZH (2021). Lipid-mediated motor-adaptor sequestration impairs axonal lysosome delivery leading to autophagic stress and dystrophy in Niemann-Pick type C. Dev Cell 56, 1452–1468.e1458.

Saleeb RS, Kavanagh DM, Dun AR, Dalgarno PA, Duncan RR (2019). A VPS33A-binding motif on syntaxin 17 controls autophagy completion in mammalian cells. J Biol Chem 294, 4188–4201.

Shen Q, Shi Y, Liu J, Su H, Huang J, Zhang Y, Peng C, Zhou T, Sun Q, Wan W, Liu W (2021). Acetylation of STX17 (syntaxin 17) controls autophagosome maturation. Autophagy 17, 1157–1169.

Shibutani ST, Yoshimori T (2014). A current perspective of autophagosome biogenesis. Cell Res 24, 58–68.
Song AH, Wang D, Chen G, Li Y, Luo J, Duan S, Poo MM (2009). A selective filter for cytoplasmic transport at the axon initial segment. Cell 136, 1148–1160.
Stavoe AK, Gopal PP, Gubas A, Tooze SA, Holzbaur EL (2019). Expression of WIPI2B counteracts age-related decline in autophagosome biogenesis in neurons. eLife 8, e44219.
Stavoe AK, Hill SE, Hall DH, Colon-Ramos DA (2016). KIF1A/UNC-104 transports ATG-9 to regulate neurodevelopment and autophagy at synapses. Dev Cell 38, 171–185.
Stavoe AKH, Holzbaur ELF (2019). Autophagy in neurons. Annu Rev Cell Dev Biol 35, 477–500.
Tsuboyama K, Koyama-Honda I, Sakamaki Y, Koike M, Morishita H, Mizushima N (2016). The ATG conjugation systems are important for degradation of the inner autophagosomal membrane. Science 354, 1036–1041.
Williams AH, O'Donnell C, Sejnowski TJ, O'Leary T (2016). Dendritic trafficking faces physiologically critical speed-precision tradeoffs. eLife 5, e20556.
Wong YC, Holzbaur EL (2015). Autophagosome dynamics in neurodegeneration at a glance. J Cell Sci 128, 1259–1267.
Yin Z, Pascual C, Klionsky DJ (2016). Autophagy: machinery and regulation. Microb Cell 3, 588–596.
Yu L, McPhee CK, Zheng L, Mardones GA, Rong Y, Peng J, Mi N, Zhao Y, Liu Z, Wan F, *et al.* (2010). Termination of autophagy and reformation of lysosomes regulated by mTOR. Nature 465, 942–946.